TASK C: EXPERIMENTAL HIGH ENERGY PHYSICS

PROGRESS REPORT

DOE/ER/40224--247

DE93 013139

Grant Number: DE-FG-85ER40224

University of Oregon

James E. Brau, Principal Investigator

DISCLAIMER

This report was prepared as an account of work sponsored by an agency of the United States Government. Neither the United States Government nor any agency thereof, nor any of their employees, makes any warranty, express or implied, or assumes any legal liability or responsibility for the accuracy, completeness, or usefulness of any information, apparatus, product, or process disclosed, or represents that its use would not infringe privately owned rights. Reference herein to any specific commercial product, process, or service by trade name, trademark, manufacturer, or otherwise does not necessarily constitute or imply its endorsement, recommendation, or favoring by the United States Government or any agency thereof. The views and opinions of authors expressed herein do not necessarily state or reflect those of the United States Government or any agency thereof.

MASTER

DISTRIBUTION OF THIS DOCUMENT IS UNLIMITED

Table of Contents
Progress Report

1. Introduction

The experimental high energy physics group at the University of Oregon broadened its effort during the past year. Having expanded to three faculty in September, 1991, with the addition of David Strom, we worked on SLD (Brau and Frey) and OPAL (Strom), GEM (Brau, Frey, and Strom) and joined the preparations for experiment E-815 at Fermilab (Brau and Frey).

The SLD effort extends from maintaining and operating the SLD luminosity monitor which was built at Oregon, to significant responsibility in physics analysis, such as event selection and background analysis for the left-right asymmetry measurement. Oregon maintains three people in residence at SLAC throughout the year, increased by two during the summer, and has others (such as Brau and Frey) commuting regularly.

The OPAL work focussed on the luminosity monitor upgrade to a silicon-tungsten calorimeter. Building on the work done at Oregon for SLD, the tungsten for this upgrade was machined by the Oregon shops and shipped to CERN for assembly.

The Oregon GEM effort now concentrates on tracking, specifically silicon tracking. Oregon also has developed a silicon strip preradiator prototype, and tested it in a Brookhaven beam.

In the Spring of 1992, Jim Brau and Ray Frey joined the E-815 Collaboration at Fermilab in its preparation for a sign-selected neutrino experiment. This experiment is scheduled to take data in 1994.

A crucial part of our proposal for next year is the request for support of three postdocs. Our plan for these three is to locate all three off site, one at SLAC working on SLD, one at CERN working on OPAL, and one at Fermilab working on E-815. We have established an extremely vigorous research program, but it is essential to maintain this effort that we have support for these positions.

Overall, the Oregon group has made very significant progress on all the research projects it has undertaken, as the following report will affirm.

2. SLD Progress Report

2.1. 1992 Run

In 1992 the SLAC Linear Collider (SLC) exceeded its pre-run goal of 10,000 polarized Z^0's, resulting in a very successful run for SLD, with encouraging prospects for the future. SLD collected over 11,000 polarized Z^0's, achieved luminosities of over 25 Z^0's per hour and 400 polarized Z^0's per day. Figure 1 summarizes the Z production during both the 1991 and 1992 runs. The significant improvements since 1991 are dramatically evident.

Polarization at SLC was achieved quite directly after a pre-polarization run of about 1,000 Z^0's into SLD. In April polarization was installed and commissioned, with a polarization level of 22-24% measured at the interaction point by April 21.

2.2. Operation of the SLD Luminosity Monitor

The SLD Luminosity Monitor, built at the University of Oregon, now operates routinely under the effort of the Oregon group. This device, a silicon-tungsten calorimeter, is pioneering the use of silicon-tungsten calorimeters in e^+e^- experiments. Both ALEPH and OPAL at LEP are installing similar systems in what may be thought of as second generation instruments, SLD's being the first generation. (Note the Oregon group through David Strom is participating in the development of the OPAL device.)

Figures 2 and 3 illustrate the SLD Luminosity Monitor (LMSAT). It is a system consisting of 23 layers of silicon pad detectors. Figure 2 shows the layout of the 300 μm thick silicon for one layer of a LMSAT module, which consists of four chips. Each module covers half the azimuth, to allow for mounting around the beampipe. The halves meet in the vertical plane, with a 1 mm offset in the active region to either side of the vertical.

Every LMSAT chip is segmented into six rings radially; the innermost two rings are "double-wide" in azimuth (2 segments per octant), while the four outer rings are more finely segmented (4 segments per octant), for a total of 20 cells per chip. All diodes were manufactured in Japan by Hamamatsu Photonics[1].

The LMSAT consists of 23 alternating layers of radiator plates and silicon chips on G10 circuit boards which are directly mounted on the radiator plates. For ease of machining, the alloy used in the radiator plates was 90% tungsten with a corresponding radiation length of 0.86 X_0 per plane. The G10 boards are mounted directly to the radiator plates. Half the boards face the IP, half face away from the IP. The gap between plates is 3.5 mm. The front face of the LMSAT is located approximately 101 cm from the interaction point. Figure 3 shows the side view of the LMSAT and the readout electronics on the SLD beamline. There is one set on either side of the IP; outgoing electrons head south, positrons north.

All diodes are reverse-biased to full depletion. Incident photons, electrons, and positrons initiate electromagnetic showers which start in the radiator plates and liberate electrons in the silicon which are in turn collected by the charge-sensitive preamplifiers. Much smaller signals are obtained from muons and non-interacting hadrons.

The first six layers of LMSAT detectors are ganged together to form EM1, while the remaining seventeen layers are read out as EM2. As explained in reference 2, the towers defined by this readout scheme are approximately projective. The detailed geometry has been implemented in SLD's version of the GEANT[3] Monte Carlo.

To monitor the effects of the radiation dose on the silicon, we installed special 1 cm^2 diodes with α sources at various locations in and around the LMSAT. The α particles produced in nuclear decays range out in the first 25 μm of silicon, and thus will give good signals only when the detector is fully depleted. A dedicated section on the instrumentation board

amplifies and multiplexes the signals from eight such diodes per side, so that the change in voltage needed to deplete the detectors can be monitored as the experiment progresses. Thermoluminescent dosimeters were also placed in and around the LMSAT. The dose for the 1991 engineering run was strongly dependent on radius from the beam line, with the maximum dose being 400 rads at the inner edge.

The electronics packages used to read out the LMSAT are mounted immediately behind the LMSAT on each side of the IP. The design is very similar to that of the SLD Liquid Argon Calorimeter (LAC) electronics, described in [4][5][6]. (Many elements, including the custom preamplifier hybrids, are identical.) Each LMSAT package, known as a "tophat", reads out 512 channels. Ribbon cables carry the signals from the detectors to the preamp boards, each of which carries four eight-channel preamps. A tophat consists of sixteen preamp boards (16 x 32=512), a fiber optic receiver/transmitter board, a controller board, an Analog-to-Digital converter board, a depletion voltage filter board, and an instrumentation board used for various monitoring functions. These boards all connect to a motherboard, which is split into upper and lower halves to allow for mounting around the beam pipe, and which provides the interconnections between boards.

The tophats receive commands from and send data out to custom Fastbus modules. A block diagram of tophat functionality is shown in Figure 4. The scheme is as follows: Signals from a Fastbus Timing and Control Module (TCM) are transmitted on optical fibers using a three-wire protocol; these signals are received and converted to TTL on the fiber optic board, and then used to generate the appropriate strobes and logic levels by the controller board. Output from the preamps is sampled immediately before and after the beam crossing in gates of width $0.75\mu s$ to provide a baseline and signal. The integrated outputs are digitized and transmitted to the Fastbus Calorimeter Data Module (CDM) in a serial stream via optical fiber. The use of optical fibers results in lower noise and greater immunity from ground loops. Each signal is carried on a redundant pair of optical fibers.

In order to minimize heat dissipation, the power to the preamps is pulsed at the SLC repetition rate of 120 Hz: the power cycles on 1 ms prior to the beam crossing, to allow time for settling, and then turns off after the beam crossing, resulting in a duty cycle of 13%. The tophat is surrounded by a sheet metal housing with a cooling loop for temperature stability.

The voltages used to deplete the silicon are supplied by special $200\,V$, $200\,\mu$A CAEN supplies which are controlled by the online Vax 8800. They are typically run at $-75\,V$. Half the CAEN channels supply 32 towers, the other half 64, with currents on the order of a few microamps per channel in the absence of shorted detector towers. Multiconductor cables bring the voltages from the sources to the filter board on the tophat; the voltages then go through the motherboards to the preamp boards, where for each tower a $1\,\mathrm{M}\Omega$ current-limiting resistor lies between the voltage source and the silicon.

A special circuit (shown schematically in Figure 5) was added ahead of the preamp for each channel which enables us to measure the voltage drop across the $1\,\mathrm{M}\Omega$ resistor due to leakage current out of the silicon. The strobe used to pulse this circuit is activated by toggling a single bit on the controller. Thus the leakage current for every tower can in principle be

measured online, although currents below a few hundred nanoamps cannot be measured reliably. This capability was designed to give useful measurements only for failing towers since normally a tower drains about 50 nanoamps.

The electronics is calibrated using circuitry built into the preamps. A precision DAC on the controller board generates a voltage in the range 0–5 V which charges laser-trimmed 8.4 pF capacitors (one per channel) in the preamp hybrid. The resulting charge is injected into the amplifier section of the hybrid, which is read out in the normal way. The CDM calculates and stores the constants obtained from a 16-point linear fit to the calibration data for each channel. Data taken during normal running are corrected using these constants to produce a "calibrated ADC" value for each channel, with 390 counts per pC of deposited charge. The CDM also applies a threshold cut before passing its data on to the Aleph Event Builder[7] (AEB).

Readout of the LMSAT is closely coupled to readout of the SLD LAC. Both systems share a single TCM and AEB. (This particular AEB is dedicated to the calorimeter subsystems and hence is known as the KAL AEB. Other subsytems, such as CRID, have separate AEBs.) Since each CDM handles two tophats, the LMSAT requires only a single CDM, compared to 28 CDMs for the LAC. The TCM and CDM functions have been described above. The KAL AEB buffers data from all the CDMs and performs clustering before passing its data on to the Trigger AEB, which receives data from all the subsystem AEBs and distributes the trigger on the Fastbus backplane.

A satisfactory Bhabha trigger for the LMSAT could be obtained by requiring a total energy of 7.5 GeV in the North detectors and 7.5 GeV in the South, with towers having less than 1 GeV suppressed. This trigger proves highly efficient for genuine Bhabha events (virtually 100%) without causing excessive dead time due to energy in the calorimeters from SLC backgrounds. These backgrounds tend to give low-energy hits in many towers, which motivated the 1 GeV threshold. Since higher backgrounds may be unavoidable in future SLC running (due to higher currents and stronger focusing of the beam near the IP), more sophisticated trigger algorithms may be necessary to minimize deadtime. The SLD trigger hardware was designed with these possibilities in mind, and can accomodate a wide variety of specifications.

Figure 6 shows the measured energy spectrum in the SLD Luminosity Monitor compared to the Monte Carlo expectation. The good agreement between data and simulation attest to the good performance of the device and the high degree of understanding of it. The Monte Carlo assumes the expected resolution of $20\%/\sqrt{E}$, which is demonstrated also by the agreement.

2.3 Physics Results from 1992 Data

The 1992 physics run of SLD has provided a sample of over 11,000 polarized Z^0's for the first physics analysis of the SLD Collaboration. To date these data have been used to study:

1. Left-right asymmetry in Z^0 production,
2. QCD effects such as α_s measurements as a function of flavor, b,c,uds fragmentation,

particle species momentum fractions vs. QCD predictions, Λ polarization, event plane orientations, and intermittency,

3. Heavy flavor physics.

2.3.1 Left-Right Asymmetry

The measurement of the left-right asymmetry A_{LR} in Z^0 production is the most significant measurement of SLD. The value of A_{LR} is simply the difference between the cross section with left-handed electrons and right handed electrons divided by the sum:

$$A_{LR} = \frac{\sigma_L - \sigma_R}{\sigma_L + \sigma_R}.$$

This measurement has many advantages as a test of the Standard Model. It is simple, clean, sensitive, and unique. Before radiative corrections, A_{LR} is related to $sin^2\theta_w$ as:

$$A_{LR} = \frac{2(1 - 4sin^2\theta_w)}{1 + (1 - 4sin^2\theta_w)^2}$$

$$\approx (1 - 4sin^2\theta_w).$$

Since the luminosity, the backgrounds, the efficiencies and the polarizations are all left-right symmetric, the measurement for SLD becomes simple counting events for each polarization state of the beam (the beam polarization is randomly reset on each crossing) to get:

$$A_{LR} = \frac{1}{P}(\frac{N_L - N_R}{N_L + N_R}).$$

The present SLD A_{LR} analysis includes 10,967 events, 5602 produced with a left-handed beam, and 5365 produced with a right-handed beam. The average beam polarization (P) is $21.9 \pm 1.5\%$. This yields a measurement of

$$A_{LR} = 0.10 \pm 0.045.$$

This measurement of A_{LR} translates into a value of

$$sin^2\theta_w = 0.237 \pm 0.006.$$

Comparison of this measurement with LEP is best done with the LEP measurements of the τ polarization. Figure 7 shows this, as presented by the LEP experiments to the Dallas Conference this summer. Here we see that the SLD error of 0.045 for the asymmetry is smaller than two of the LEP experiments and larger than two.

2.3.2 QCD

The SLD experiment has presented QCD analysis on its data at several conferences. The most advanced analysis is on jet rates and energy-energy correlations, to measure the value of α_s. The values extracted for each of these methods are:

Jet rates:

$$\alpha_s = 0.119 \pm 0.002 \pm 0.003 \pm 0.014$$

Energy-energy correlation:

$$\alpha_s = 0.121 \pm 0.002 \pm 0.004 \pm \begin{matrix} 0.016 \\ 0.009 \end{matrix}$$

asymmetry of the energy-energy correlation:

$$\alpha_s = 0.108 \pm 0.003 \pm 0.005 \pm \begin{matrix} 0.008 \\ 0.003 \end{matrix}.$$

In each case, the errors given are statistical, systematic, and theoretical, respectively.

Figure 8 shows the SLD measured jet fractions. Figures 9 and 10 show the energy-energy correlations and the asymmetry in the energy-energy correlation. These results are already quite competitive to LEP in that such measurements have large theoretical errors, which higher statistics cannot overcome.

In addition to these QCD studies, the Oregon group has been instrumental in studying intermittency in the SLD data. Intermittency studies involve the multi-particle dynamics of hadronic final states. The basic idea is to look for non-Poissonian fluctuations in the multiplicity density of charged particles in rapidity and/or azimuth, to determine if the physics underlying the fluctuations can be understood in terms which are more satisfactory than the present phenomenological descriptions, for example like that of the LUND monte carlo program. To date, the connections between particle production and QCD have been little understood. The goal here is to understand the dynamics of QCD using a fresh and promising approach. For the most part, experimental studies of intermittency are not statistics limited. The sample of $\approx$ 50K hadronic Z events available over the next year with SLD will be adequate for almost everything we hope to accomplish, most of which has not been undertaken by any of the LEP groups.

2.3.3 Heavy Flavor Physics

The SLD experiment has some competitive advantages over the LEP detectors in its ability to study heavy flavor physics. The excellent SLD vertex detector provided by the CCD system located just 2.5 cm from the IP, combined with the powerful particle identification made possible by the SLD CRID, system give SLD the ability to tag heavy flavors with high

efficiencies and low systematic errors. The polarized electron beam adds an additional tool to the arsenal. Finally, the small SLD interaction spot sizes are very useful.

Table 1 shows the comparison of the SLD vertex detector capabilities to those of LEP, emphasizing the strengths of SLD. As an illustration of the first results from this data, Figure 11 shows the impact parameter distribution of the data. The upper figure is for all good vertex tracks, the center figure of the tracks from events of the 1-1 topology and the bottom figure from the 1-3 topology. From Monte Carlo we expect 21.5 events in the 1-3 topology and we see 17, demonstrating that the analysis software and the detector are working. The extracted τ lifetime is 289 ± 67 fsec.

ISSUE	SLD/SLC	LEP
Effective IP Size	2μm X 2μm X 650μm	15μm X 200μm X 1.8cm
Tracking Inner Radius	25mm→40mm	65→100mm
Precision Tracking (now)	CCD Pixel Vertex Det.	ALEPH - Si. Vtx. (2X Rφ,Z) DELPHI - Si Strips OPAL - Si Installed (?) L3 - Vtx./Drift
Impact Resolution (XY)	expect: $\approx 12.8\mu m \oplus \frac{70\mu m}{p\sqrt{\sin^3\theta}}$ (30μm⊕ now; expt. 15μm ⊕ after known dstrtns removed)	eg: $30\mu m \oplus \frac{70\mu m}{p\sqrt{\sin^3\theta}}$ (DELPHI) (ALEPH 13μm⊕...)
Impact Resolution (Z)	$\approx 35.4\mu m \oplus \frac{65\mu m}{p\sqrt{\sin^3\theta}}$ (75μm⊕ now; 58μm ⊕ after known dstrtns removed)	ALEPH HAS 2 LAYERS OF (Rφ,Z)
Event to Event IP Size	Stability « 15 μm Pri.Vtx. ≈ 35μm in XY,Z	Centroid Stability « 20 μm Pri.Vtx. ≈ 50μm in XY Guess (150 μm in Z ?)
Hadron ID	Barrel & Endcap CRID	Only DELPHI Had RICH

Table 1.
SLD/SLC/LEP Comparison

With the SLD silicon pixel vertex detector hardware and software fully operational, many physics studies are possible. Many of the topics will not be limited by statistics at SLD or LEP, but by systematics and the SLD close-in pixel detector, complemented by the particle identification of the CRID, will be very competitive. We expect to contribute to the following topics:

- $\Gamma(Z^0 \rightarrow b\bar{b})$
- A_b (From improved A_{FB})
- A_{FB} (With Polarized Electrons)
- b-Lifetime
- τ-Lifetime

3. OPAL Progress Report

3.1 Luminosity Monitor

Since the start of Z^0 physics at LEP in 1989, the experiments have recorded increasingly large samples of Z^0 decays. About one year ago it was recognized that despite numerous small upgrades to the OPAL luminosity monitor, it would be difficult to use efficiently the large data samples expected at LEP. Approximately 10^6 Z^0 bosons which are expected by the end of the current run and roughly 2.5×10^6 are expected by the end of the first phase of LEP. In order to keep the error on the luminosity similar to the expected experimental error on the acceptance corrected number of Z^0 leptonic and hadronic decays, a number of institutions in the OPAL Collaboration, including the University of Oregon, proposed to build a silicon-tungsten calorimeter monitor capable of measuring the LEP luminosity to 0.1%[8]. The 0.1% goal is also consistent with the theoretical error on the small angle Bhabha cross section[9].

The decision to build a silicon-tungsten calorimeter was based on the necessity to use a calorimetric technique to measure the energy of outgoing electrons and positrons from Bhabha scattering, but at the same time to define the angular acceptance of the luminosity measurement with a sufficient precision so that the goal of 0.1% measurement could be reached. An advantage of a calorimetric position measurement is that it can be directly compared with a leading log calculation of the small angle Bhabha cross section.

The new detector consists of two annular calorimeters 22 radiation lengths deep. Each calorimeter is longitudinally segmented with 14 one radiation length samplings and 4 two radiation length samplings. The silicon detectors are segmented into radial pads with a radial pitch of 2.5 mm corresponding to about 1 milliradian in polar angle and an azimuthal pitch of 11.25°. Each pad is separately readout using a custom integrated circuit which multiplexes 16 channels to a single output. Details of all aspects of the construction of the new luminosity monitor can be found in the OPAL proposal given to the LEPC[8]. Here we concentrate on those areas which benefited most from University of Oregon involvement.

3.2 Position Resolution and Silicon Detectors

Silicon detectors are an ideal sense media because of the accuracy with which the geometry of the sensitive area of the silicon may be defined. The systematic error associated with the measurement of the small angle cross section is often limited by the determination of the inner edge of the detector's acceptance. The inner edge is important because the small angle Bhabha scattering cross section is proportional to $1/\theta^3$. In order to have the acceptance independent of the azimuthal angle, ϕ, a geometry with circular pad rows was chosen. For a luminosity measurement based on the region 30 mr $< \theta <$ 50 mr, the coverage of the new OPAL luminosity monitor, a simple calculation shows that the systematic error on the inner edges of the acceptance must be less than 10 μr. At a distance of 2 meters from the interaction-region this equivalent to 20 μm on the radial distance of a given pad from the interaction region. Fortunately the geometry of silicon pad detectors can be defined at the micron level, so the main challenge is to place the silicon detectors so that their pad rows are aligned to better than 20 μm in radius. It should be pointed out that the two sides of the luminosity monitor need not be aligned with each other with a precision of 20 μm because any rigid shift in the position of one of the calorimeter will only effect the luminosity measurement to second order. The distance between the two calorimeters is a crucial parameter; the 0.1% goal requires that the distance between the two calorimeters be know to better than 1 mm.

The University of Oregon group took an active role from the beginning in the design of the new detector. The experience of the SLD group was especially helpful in the design of the silicon detectors themselves. Using startup funds, we were able to order the first prototypes at the end of 1991 from Hamamatsu. These prototypes were delivered in March of 1992. These detectors were found to have especially low leakage current, typically less than 2na/pad, and to exhibit no increase in leakage current after being glued to a ceramic circuit board. Based on our good experience with the prototypes, an order for the 700 detectors needed for the final calorimeter was placed with Hamamatsu.

3.3 Energy Resolution and Sampling

The energy resolution of the luminosity monitor must be sufficient to separate coincident off-momentum background electrons and positrons from genuine Bhabha events. At polar angles above 50 mr (the fiducial acceptance of the present luminosity calorimeter) the background from accidentals is less than 0.01%. At smaller angles the off–momentum background is expected to increase and to be closer in energy to the signal. This is because the Minibeta Quadrupoles act as spectrometers for off–momentum background and deflect the lowest energy particles through the largest angles. Figure 12 shows the behavior of the background in OPAL and L3 as a function of the angle and energy cut. To keep the background at an acceptable level, an energy cut of $0.85E_{beam}$ may be needed. For a Gaussian energy resolution of 3%, much less than 0.1% of beam energy electrons or positrons are cut by this requirement. The Non-Gaussian tails on the energy resolution can be studied by selecting back to back Bhabha events which have little initial state radiation. The energy resolution of a Silicon-Tungsten electromagnetic calorimeter is given by $0.20\sqrt{\frac{X}{E}}$ where X is the sampling in units of radiation lengths. We chose to have 14 one–radiation–length samplings followed by 4 two–radiation–length samplings.

Each of the calorimeters in the luminosity monitor consist of two halves which are brought together around the beam pipe. A gap of 100 μm is left to allow some tolerance for the gluing of the tungsten plates to their aluminum support rings. To avoid having a small region in azimuth which will be not be usable for the luminosity measurement, alternate layers of the detector are offset in azimuth by 5.625°. The effect of these gaps is further mitigated, by machining the tungsten with a 30° beveled inner edge.

The 60 one–radiation–length and 20 two–radiation–length tungsten blanks were procured by the University of Oregon during the spring of 1992. These were ground by a local firm to have constant thickness to better than 1%. The ground plates were then machined into half rings by the University shops. The first quarter of the tungsten, enough for one half calorimeter was delivered to CERN at the end of June, in time to be used in the test run of a partially assembled luminosity monitor. The remaining tungsten was delivered to CERN by the end of the summer.

3.4 Beam Test

Test beam time was scheduled at the CERN SPS for August of 1992 to allow the test to be carried out on a partially completed calorimeter. One motivation for the test was the observation by other groups of local hardening in electromagnetic showers[10]. This effect is due to the absorption of the soft component of the electromagnetic shower by material directly before or behind the Silicon. An especially large effect was predicted by the GEANT Monte Carlo, while almost no effect was seen in EGS. Because of the lack of agreement between the two simulations, it was decided to measure the response of the silicon with ceramic in front of the silicon and with the ceramic in back. An especially important point for investigation is shower size. Since the hard part of the shower most accurately reflect the position of the electromagnetic shower, a geometry which enhances the hard part of the shower is advantageous.

The major contribution of University of Oregon to the test beam effort was in supplying the online software needed for the test. This software was developed for a VME OS9 based system in the spring of 1992 at the University of Oregon and then refined at CERN during June of 1992. The software was structured so that it could be also used for the test of the GEM preradiator at the Brookhaven AGS in July.

The timing of the test beam was such that prototype electronics from the entire readout chain were available. The silicon wafers were glued and bonded to a preproduction series of the ceramic circuit boards, which included four AMPLEX dice. The AMPLEX chip was designed originally for the readout of the UA2 micro-vertex detector. It was modified subsequently for use with the ALEPH silicon-tungsten luminosity monitor to include a trigger output and an improved dynamic range. For use with the OPAL calorimeter an additional modification was made in order to provide additional protection against damage from electrostatic-discharge during detector assembly. Each AMPLEX die contains 16 sample and hold circuits, which are multiplexed to a common output. The outputs from the four AMPLEX dice are multiplexed further to a single analog output for each ceramic circuit board. This output was

then digitized using custom VME digitizers provided by the University of Chicago. These digitizers each contain a single 14 bit ADC.

At the time of the test beam, sufficient electronics existed to instrument three ceramic boards on four layers of the detector. We chose to instrument the calorimeter with a bare layer of silicon, followed by sampling at 4, 6 and 8 radiation lengths. To test the sensitivity to the orientation of the silicon detectors, the entire detector could be rotated by 180° to give sampling at 4,6,8 and 12 radiation lengths.

3.5 Test Beam Results

The detector was installed in the test beam late on August 7th and by August 9th we were able to see very clean signals from a muon beam. Figure 13 shows the pulse height distribution for muons hitting a single pad. The most probable value was equivalent to approximately 24,000 electrons. The pedestal had an RMS noise of about 2 ADC counts, giving a signal -to-noise ratio of about 10 to 1. The low level of noise was especially encouraging since 2 ADC counts corresponds to an analog signal from the AMPLEX chip of just 0.6 mV. When running with electrons at 45 GeV a signal, summing over all pads at shower maximum, of about 6,000 ADC counts was observed, well within the range of the 14 bit ADC.

A major goal of the test beam effort was to determine the shower profile. Figure 14 shows the shower profile as a function of radial pad number. It can be seen that the core of the shower is concentrated in a single pad for all but the the last sampling. This figure justifies our choice of a small radial pad size of 2.5 mm. The optimum detector orientation is still under study, as the precise shower profile requires that cross talk and calibration be understood at the 1% level.

After we had completed taking the data needed to address the issues posed by the local hardening effect, the remaining test beam time was devoted to studies of position of the detector. It had originally been planned to study position effects in a 1993 test beam run together with the OPAL microvertex detector group, however, it was realized that much useful information could be gleaned from a setup with two orthogonal layers of microvertex detectors. To study the position resolution of the detector, the bare layer of silicon was replaced by two ceramics which had been configured to readout a silicon-microstrip detector with a pitch of 50 μm. Using these detectors together with three upstream delay wire chambers, it is possible to reconstruct the trajectory of electrons and muons through the detector at the 20 μm level. It was necessary to use muons in order to determine the relative alignment of the microstrip detectors to the silicon pads inside the calorimeter. The muons, did provide a check of the relative alignment of the various layers of the detector, showing that they had been positioned with an accuracy of 20 μm. The final measurement system for verifying the position of the silicon detectors was not yet in place, so this result was to some extent fortuitous.

Figure 15 shows the response of the detector to muons and electrons near one of the pad boundaries. It can be seen that the muons can be used to survey the pad detectors at the 20 μm level. The resolution of the detector at the pad boundaries for electromagnetic

particles can be seen to be about 150 μm. In order to reach the 0.1% goal on the systematic error there must no bias to the reconstructed shower position at the 20 μm level. The effect of the resolution on the reconstructed shower position is a second order effect which can be corrected, if the resolution is known. A slight inward bias of the reconstructed shower position is introduced due to the finite size of the shower and the radial pad layout. This bias is proportional to s^2/r where s is the shower size and r is the radius of the pad row. The magnitude of the effect depends on the shower size which is narrow at the beginning of the shower evolution. An effort to evaluate the size of this bias using the test beam data is currently underway.

Additional test beam data was taken to study the effect of material between the detector and the interaction point. For these runs the silicon micro-strip detectors were located upstream of a simulated beam pipe.

3.6 Detector Construction and Assembly

The assembly of the new luminosity monitor is presently underway at CERN. Testing of the AMPLEX chips and Silicon detector is complete. Production of the ceramic circuit board and associated electronics is underway at CERN with the aim of completing the assembly of the detector by the end of 1992. Installation of the new luminosity monitor in the OPAL experiment will occur in April of 1993, prior to the start of the 1993 LEP run.

4. GEM Progress Report

The Superconducting Super Collider(SSC) provides an enormous increase in the center of mass energy of colliding beam experiments. The discoveries from this new era of exploration may include the origin of the masses of the $W^{\pm}$ and Z^0, the origin of mass of quarks and leptons, the top quark, perhaps the discovery of speculated new particles of the supersymmetry theory, or many other possible anticipated phenomena. The GEM detector has been designed to discover these new physics, and once discovered, to study them in great detail. It is also possibile that the GEM detector at the SSC will discover totally unexpected new effects, providing the most exciting scenario of all. Whatever the outcome of this great adventure, science will step deeper into the structure of matter and our understanding of our universe, its origin, and its future will advance.

During the past year the GEM effort of the Oregon group has moved from calorimetry to tracking. In the Fall of 1991, Jim Brau served as co-leader of the GEM Calorimetry Group and lead the calorimetry effort through to the submission of the GEM Letter of Intent. During this time, the group also was working on the development of a silicon strip preradiator for GEM. In early 1992, the Oregon group joined the GEM Central Tracking Group, and began to redirect its effort from calorimetry to tracking. Since then the effort has been split between continued development of a silicon preradiator and the silicon microstrip subsystem of the GEM central tracker. A preradiator would enhance the GEM detector's capability to search for the Higgs boson in the intermediate mass range (80-140 GeV/c^2) through the

two photon decay. This search demands exceptional rejection of the enormous background from the two jet and jet-hard photon events which outnumber the signal by many orders of magnitude [11]. The Oregon group led the development of the silicon strip preradiator. This included the simulation of the preradiator performance and requirements, construction of a prototype, and testing of the prototype at Brookhaven National Laboratory in July of 1992.

During 1993-94, the Oregon effort will concentrate on GEM tracking. This will include studies of the complete tracking system performance, but will primarily concentrate on the silicon microstrip subsystem. The Oregon group has assumed responsibility for the silicon detector development, specification, and procurement. Additionally, Oregon will work on the development of the microstrip readout electronics.

4.1 GEM Physics Motivation, Detector Philosophy

The primary motivation for the construction of a 40 TeV hadron collider (the SSC) is to explore electroweak symmetry breaking — the origin of the masses of the gauge bosons and the quarks and leptons.[12] While the source of this symmetry breaking is unknown, the mass scale is not. For example, the strong interactions of the longitudinal components of the vector bosons must increase, violating unitarity in the 1 - 2 TeV range, unless a new mechanism suppresses them. The standard model is finite and renormalizable, due to the existence of a scalar Higgs singlet. Supersymmetric models predict a host of new particles with well defined interactions and decays but undetermined masses. Technicolor and other dynamical symmetry breaking mechanisms replace the elementary Higgs mechanisms with composite particles. Many of these predicted new particles produce W's and Z's in their decay chains. Signatures for the production and decay of supersymmetric particles include events with like sign leptons or events with jets and missing p_T and no leptons. If the standard Higgs, supersymmetry, or technicolor models are not correct, other possibilities include the emergence of strong interactions between boson pairs with masses in the 1 - 2 TeV range [13] and the possibility of a heavy top (around 200 GeV) condensate playing the role of the Higgs.[14]

The common thread that links these physics objectives is the presence of the intermediate bosons (the $W^{\pm}$, Z^0 and the photon) and their decay products, the electrons, muons, jets, and neutrinos, which also constitute the fundamental probes of high energy collisions. A detector that is capable of providing an optimized and balanced emphasis on all of these probes will provide the broadest attack on this physics. Furthermore, if these goals are accomplished, the detector can address new and unexpected phenomena through the leptons. In order to cope with the challenges of the SSC, the GEM design seeks to optimize the detector through outstanding performance over the full solid angle, with excellent resolution for electrons, muons, jets, and neutrinos, while maintaining the capability to run at very high luminosity.

Since the principal physics justification for the SSC is the elucidation of the electroweak symmetry breaking (the central physics focus of the GEM Detector), the search for the Higgs boson or bosons and searches for other competing symmetry breaking mechanisms (technicolor or supersymmetry) are the main focus. Additionally, searches for new quarks,

leptons, Z's, W's, substructure, or other unexpected new phenomena are planned.

With these physics goals in mind, the design of the GEM detector has led to the following characteristics to maintain complementarity to SDC:

1. Precision muon momentum measurement in an open geometry outside the calorimeter;
2. High precision electromagnetic calorimetry, without the handicap of an inner magnetic coil;
3. Hermetic, projective hadronic calorimetry with adequate energy resolution ($\sim 50\%/\sqrt{E}$);
4. Central tracking in the magnetic field.

The GEM design incorporates a tracking system based on silicon strips and interpolating pad chambers. The tracking system occupies a volume of 0.75 m in radius and 3 m in length. Surrounding the tracker is a volume for calorimetry, 3.6 m in radius and 12.5 m in length. The GEM electromagnetic calorimeter will be an accordian liquid krypton calorimeter with the best resolution possible, with confidence at the SSC ($\frac{\sigma}{E} \sim \frac{6.5\%}{\sqrt{E}} \oplus 0.4\%$). The hadron calorimeter has not been fully specified at the time of this writing. Beyond the calorimetry are measuring stations for muon trajectories, within the open field of the roughly 20 m diameter superconducting solenoidal magnet.

4.2 GEM Silicon Preradiator

During the past year the Oregon group has been studying a silicon preradiator for possible use in the GEM detector. These studies have included simulations of performance, design and fabrication of a prototype device, and its test in a beam at Brookhaven National Laboratory in July 1992. We describe these issues below and present some of the results of the analysis of the test beam data.

4.2.1 SSC Physics Goals and the Role of a Preradiator

The potential of lepton and single γ identification as physics tags motivates the deployment of a preradiator at the SSC. Numerous physics goals benefit from this subsystem: heavy Higgs, intermediate mass Higgs, top searches and studies, direct photon production, as well as more exotic studies such as Z' and heavy quarks. The excellent electron identification and π^0 rejection of the preradiator could contribute significantly to these physics studies. Most significant for GEM is the role of the preradiator for enhancing the $H \rightarrow \gamma\gamma$ signal for a Higgs boson of intermediate mass. The preradiator would help to distinguish between single photons (from $H \rightarrow \gamma\gamma$) and photon pairs from π^0 decay in (background) multi-jet events.

Consider the GEM calorimeter with a silicon strip preradiator. The pixel structure of a silicon strip preradiator offers important advantages over other techniques in electron/hadron rejection. The overlap of complicated events, for example, is much simplified with a pixel detector. A "pixel" here would have a rectangular shape with dimensions of approximately

1 mm × 50 mm.

A silicon preradiator deployed in front of the GEM calorimeter would enhance considerably the capability for identification and measurement of electrons and photons. Such a preradiator could determine the centroid of an electromagnetic shower with a precision of better than 0.5 mm in both transverse coordinates. Additionally, the signature for two overlapping electromagnetic showers (the signature of a π^0) would be observable in many cases. The main advantages of a preradiator would be:

- Discrimination of single γ's from π^0's by observing the origination of both showers in the π^0 case.
- Reduction of the $\pi^\pm$ contamination in the electron sample by at least a factor of 10 over bare calorimeter cuts by discriminating against charged tracks which deposit very little energy in the preradiator.
- Suppression of electron sample contamination by the accidental overlap of charged tracks with γ's by detecting a small displacement between the charged track trajectory and the origin of the shower.
- Enhancement of the tagging of b-quark jets by electrons by resolving electron showers even when they are comparatively close to the jet axis.
- Measurement of the direction of γ's by combining the preradiator measurement of the initiation point of γ induced showers with the shower centroid from the calorimeter.
- Tagging of the beam crossing bucket for an electromagnetic shower.

Several technologies have been put forth for preradiator subsystems. The advantages that a silicon strip system offers are:

- Pad/strip structure– no ghosts or shadowing
- Projective in 2D
- Spatial resolution < 0.5 mm
- Two track resolution ~ 3.0 mm
- Fast (single bunch response)
- Only ~15k readout channels

The unfavorable attributes are:

- Specialized readout (limited to 3-4 bits/channel) to be developed
- Multiplexing required for 15k readout channels
- Two track resolution ~ 3.0 mm (limits π^0 veto)

A preradiator detector samples an electromagnetic cascade while introducing a minimal

interaction probability, to use the well-defined development of electromagnetic cascades to eliminate hadrons. A preshower detector that emphasizes both longitudinal and transverse shower definition is clearly more powerful than one which chooses only longitudinal. By similar reasoning one which uses two-dimensional transverse shower size information is more powerful than one which operates in projection. The two-dimensional shape information allows one to detect e/γ overlaps as well as the unpleasant cases in which a pion undergoes a charge-exchange reaction in the first converter plate, giving a lovely electromagnetic cascade, but with a p_T kick away from the incident direction. The GEM Collaboration must strive to devise a robust electron detector over the entire energy range of interest (50 GeV – 5 TeV) with sufficiently redundant electron identification power on "normal" events so that the rare events of interest in the SSC can be tagged unambiguously.

This argues in favor of a silicon strip preradiator detector. The two dimensional information will be a powerful additional handle for electron tagging within high-p_T jets, compared with projective devices. The collection speed and rate capabilities of silicon are very important in the SSC environment. Moreover, the charged particle flux in the SSC produces negligible radiation damage. Only the albedo neutron flux must be tolerated, and the silicon detectors may be less sensitive than the tracking devices and readout, depending on choices for the detector.

To reiterate, the strengths of silicon are:

- ease of segmentation into arbitrary pixel geometry
- fast silicon signal collection to minimize event pileup
- pixel geometry to minimize pileup within one interaction
- absolute gain calibration, uniform throughout the detector
- minimal support and readout needs

In the early stages of shower buildup the transverse spread of the electromagnetic cascade about the incoming particle direction is limited to a small fraction of the Moliere radius that describes the mature cascade. This tight energy cluster is an important signature of an electron, and it also serves to aid in isolating electron candidates within a jet. Projective devices, for example, have more trouble with hadron/photon pileup within a jet. A two-dimensional measurement will give maximum rejection power.

The electronics for the silicon preshower detector can be simpler than for the full calorimeter. The dynamic range is lower and the capacitance is smaller. The charge is lower, so the ADC can be simpler, faster, and lower power than for the calorimeter in general, with fewer bits. There will be enough channels in the device to warrant dedicated electronics. The cost should be cheaper for silicon than for other detector candidates, since less signal processing is required on the preamp outputs to achieve the speed required. During the past year initial electronics designs were put forth. The most promising scenario, both for performance and cost, involved local digitization in about 4 bits, local digital pipelining, followed by digital multiplexing to the outside. A reduction of digitizing channels was found in principle to be

possible by ganging channels separated by a certain number of strips (e.g. 8) to a single ADC channel. Unfolding the ambiguities in this case could be accomplished by comparing to the calorimeter.

4.2.2 Simulation of the Preradiator

Although the preradiator will serve a very important role in electron identification, its function in rejection of π^0 backgrounds is crucial and very challenging. For example, π^0 background rejection demanded by the search for the intermediate mass Higgs boson in its decay to two photons requires stellar performance. We choose this process as a benchmark to assess the performance of the preradiator.

Figure 16 presents a few important distributions in the $H \rightarrow \gamma\gamma$ process for a 100 GeV Higgs. These plots show the gamma energies, the gamma pseudorapidities, the gamma transverse momenta, and the correlation of gamma energy with pseudorapidity. We note that a cutoff in pseudorapidity at 2.5 truncates the high end of the energy distribution.

Figure 17 shows the optimal rejection power of a preradiator that requires separation of the two gammas by 2, 3, or 6 mm in x or y as a function of the π^0 momentum divided by the pathlength from the π^0 decay to the preradiator. Also shown is the histogram for the γ's produced in the 100 GeV Higgs decay to $\gamma\gamma$ to illustrate the region of required coverage. One sees the need for a system which is able to reject at the 3 mm level.

Figures 18 and 19 present the pulseheight profiles for 50 GeV π^0s decaying with the minimal opening angle. This corresponds to the GEM configuration at about $\eta = 1.0$. The bin size is 0.2 mm. Figure 18 shows the first four such events generated to give some feeling for the event-to-event fluctuation and figure 19 shows the distribution for a sum of 500 events. Magnetic field effects have been neglected in these studies.

4.2.3 Preradiator Prototype

Our device consists of tungsten radiator followed by two layers (X and Y) of silicon detectors. The typical tungsten thickness is three radiation lengths. The silicon detectors are of length 48 mm and pitch 1mm. The readout is achieved by low-noise, low-power custom preamplifier chips mounted directly on the detectors via custom circuit boards. This preradiator, with 50 cm of lead-glass behind it, was tested in a beam at Brookhaven National Laboratory (BNL) in July 1992. The details follow. While the device we built allowed for tests of the essential aspects of an SSC preradiator (e.g., detector size and segmentation, and preamplifier design), it was not a technical prototype of a real SSC device. In particular, the engineering for a compact electronics layout, local digitization, and electronics cooling and mounting were ignored at this stage of evaluation.

The silicon detector diodes making up the strip preradiator are Hamamatsu type S2461. Each such detector is 48 mm × 48 mm, segmented into 48 strips of 1 mm pitch and 0.9 mm width. The silicon wafer thickness is 0.3 mm. Each strip has capacitance $\approx$40 pF. The detectors become fully depleted at about 70 Volts. The principle of connection is shown in

Fig. 20. Note that in our case the bias voltage is positive, and is applied to the detector side opposite of the readout. This has the advantage of allowing the preamplifiers to be directly DC-coupled to the detectors. The potential disadvantage of this scheme in a large application is that an extremely high leakage current in one strip could jeopardize an entire detector. We have experienced no difficulties of this type.

The preamplifier used for the strip readout[15] was a monolithic, bipolar, "folded cascode" design with a JFET input stage. The design is due to the Oak Ridge group as part of the SECC SSC sub-system project. The specific design employed for the strips was designated FC1X1, and was designed for a detector capacitance of ≈30 pF. These custom chips were fabricated with four channels per 7 mm × 9 mm × 2 mm package. The feedback capacitor for the FC1X1 is 10 pF, for a gain of 100 mV per pC input. The equivalent noise is 4500 RMS electrons at room temperature (for a 27 pF detector). The rise time is 4 ns. The power consumption is 18 mW per channel. The preamps are designed to drive signals for not much more that ≈1 m. We note that these preamplifiers were originally designed for silicon electromagnetic calorimeters (as part of the SECC project) rather than preradiators. On average the shower development in the preradiator is considerably less than a full calorimeter. Hence a design made specifically for a preradiator would be somewhat different, with an increased sensitivity. A set of shaper/driver channels was employed for our test. These were slower, more conventional channels, also designed and built at Oak Ridge, with a shaping time of ≈50 ns and a voltage gain of ≈40.

Figure 21 shows the positions of silicon detectors and preamplifier chips as mounted on the readout printed circuit board. The detectors were fastened with conductive epoxy to the boards, thus allowing application of the positive bias voltage. Wire bonding provided the connections of the strips to the readout board. For mechanical stabilty, the readout board is 1 mm thick G10. The readout boards were designed to accommodate either an X or Y-strip orientation. X-strip and a Y-strip boards were attached back-to-front to make a single rectangular unit, with the outputs from X-strip preamps and Y-strip preamps exiting the unit at opposite ends. About 50-100 cm of cable connected these outputs to the shaper electronics. In the test at BNL, the outputs of the shapers were passed to LRS FERA ADCs (0.25 pC/count) via 100 feet of flat 100 Ω ribbon cable.

Figure 22 depicts the overall configuration of the beam test. One to three tungsten plates, each of thickness 1 radiation length (1 X_0 = 3.5mm) were placed directly before the silicon detector unit. A 3×4 -block array of lead glass, part of that previously used in BNL experiment E865, was stacked behind the silicon detectors. Each of the lead glass blocks had dimensions 6.4 cm × 6.4 cm × 50 cm. The lead glass blocks were readout into an LRS 2249A ADC. The electron trigger was provided by a coincidence of two upstream Cerenkov detectors and a pair of plastic scintillators just before the preradiator prototype. We estimate our data triggers to be ≈ 95% electrons. The data acquisiton was performed by a VME-based MVME 68040 processor manufactured by CES.

The data taking was limited to a two day period. Data was taken at 2, 4, and 5 GeV, mostly with electron triggers, although some pion data for calibration was also taken. In addition

to separate pedestal runs, pedestal events were also taken out of time with the beam spill. Data was taken with 0, 1, and 3 radiation lengths of tungsten in front of the silicon. A run was also made with 4 cm of aluminum between the preradiator and the lead glass in order to simulate the effect of a dewar wall.

4.2.4 Preradiator Beam Test Results

The test beam results are organized below into two sections which reflect the two important questions for the physics performance of an SSC preradiator:

1. Can the case of one electromagnetic shower be readily distinguished from the case of two or more showers which are nearby in space?
2. What effect does the preradiator have on the energy resolution of the electromagnetic calorimeter?

First, we present some basic distributions. Fig. 23 gives the pulse height distributions for the silicon strips under different conditions. Fig. 23 (a) is for a pedestal run. This shows that the RMS noise is roughly 3 ADC counts. (It should be noted that we had to correct all the data for a degree of coherent noise pickup. Because of the short period allotted for data taking, we had little opportunity to correct the coherent pickup in the hardware, but we have been able to readily correct for it offline because of the high degree of correlation between channels.) This can be compared to a single MIP, which is expected to be 10 ADC counts on average. The MIP signal can, in fact, be seen in the next plot (b) of Fig. 23, which is for a run with no radiator in front of the silicon strips. Plots (c) and (d) are for runs with 1 X_0 and 3 X_0 of tungsten, respectively. One can clearly see the measurement of localized electromagnetic showers. Because the 5 GeV beam was the highest available to us on the A2 beam line, we focus below on the 5 GeV electron data with 3 X_0 of tungsten radiator.

4.2.5 Shower Spatial Distribution

Fig. 24 gives event displays for the first 6 events of a run with 5 GeV electrons and 3 X_0 of tungsten. These displays give pulse height (measured charge in ADC counts) versus strip number. The X-strips are numbered 1–48, and the Y-strips are 49–96. One ADC count corresponds to about 12 KeV of deposited energy. One sees that while the 5 GeV electron showers are not as substantial as those expected for energies relevant for an SSC preradiator, they still appear to be reasonably well-defined in transverse profile. In lieu of a high energy electron beam, the important question is how well the 5 GeV showers can be modelled by the EGS monte carlo, and hence allow for an extrapolation to higher energy to be made with some confidence.

Figure 25 is the averaged shower profile obtained from the event displays by placing the strip with maximum pulse height at the center of the distribution. The squares represent about 2800 beam events, while the histogram is the corresponding EGS simulation (100 monte carlo events). One can see reasonably good agreement. We note that agreement at this level

requires some care in the EGS description of the geometry, as well as to account for the effect of albedo from the lead glass array behind the preradiator.

While the average shower profile of figure 25 agrees well with EGS, it is also necessary to examine in detail the profiles of individual events. Decisions from a pattern recognition algorithm used to distinguish between single showers and nearby multi-showers are based on single events.

Figure 26 shows the number of strips above some threshold as a function of that threshold for both data and for the EGS simulation. Again there is reasonably good agreement, indicating that the pattern of energy distribution in individual events is in reasonably well described by EGS. We are presently continuing these comparisons by using simple algorithms to identify clusters, as opposed to single strips. This will represent more closely what can be expected for a real device.

4.2.6 Energy Resolution and Correction

While a preradiator may be very useful where a highly granular electromagnetic presampler is important, especially for identifying multi-particle showers as discussed above, one must decide if this benefit is outweighed by the effect of the preradiator on the overall energy resolution of the electromagnetic calorimeter. We use the present data to demonstrate that the energy deposited in the preradiator can be used to correct the calorimeter resolution in a straightforward way.

In the BNL test, the electromagnetic calorimeter consisted of a lead glass array, as described above. By taking data with no material before the lead glass, we obtained its energy resolution. Unfortunately, we did not have an opportunity to do a good block-to-block calibration of the array. Hence the energy resolution of the entire array is not better than that of the central lead glass block. Therefore we use only the central block in this discussion.

Figure 27 shows the measured correlation between the silicon response and the response of the center lead glass block. The correlation between the two is used to make the energy correction: $E = E_0 + < E_W > + G(E_{Si} - < E_{Si} >)$, where E and E_0 are the corrected and uncorrected lead glass energies, respectively, $< E_W >$ is the average energy deposited in the tungsten radiator, E_{Si} is the silicon energy, and G is the slope indicated by the correlation plot in figure 27. All energy distributions were fit by gaussian distributions, and the resulting resolutions are given in Table 2, next page.

One can see that a substantial correction can be made to the energy resolution using the preradiator information and that this correction seems to be well-modelled by an EGS simulation. For completeness, we include resolutions from the EGS simulations for a full lead glass array (i.e., complete shower containment) for 5 GeV electrons as well as for 50 GeV electrons, in Table 3.

Table 2
One-block lead glass resolution for 5 GeV electrons for data and EGS simulation. Errors are 10% .

	σ_E/E (%) - Data	σ_E/E (%) - EGS
No Preradiator	3.2	-
3 X_0 W - no correction	4.8	4.9
3 X_0 W - corrected	4.1	4.1

Table 3
EGS simulation results for resolutions with and without preradiator correction for a full lead glass array for 5 and 50 GeV electrons.

	σ_E/E (%), 5 GeV	σ_E/E (%), 50 GeV
3 X_0 W - no correction	3.6	1.1
3 X_0 W - corrected	2.6	0.8

4.3. GEM Central Tracker

The Oregon group joined the GEM central tracker group in February, 1992 and works on the development, fabrication, and commissioning of the silicon microstrip system.

4.3.1 General Description of GEM Central Tracker [16]

The central tracker of the GEM detector is designed to operate in the 0.8 Tesla magnetic field of the large GEM superconducting solenoid. The tracker is compact, with a 75 cm outer radius and a total length of 300 cm. It covers a pseudorapidity range of $\pm$ 2.5 units. The present baseline design consists of a Silicon Microstrip (SM) inner tracker and an Interpolating Pad Chamber (IPC) outer tracker. The geometry of the Central Tracker in this design is shown in figure 28.

A variety of technologies were considered for use in the GEM Central Tracker. For the inner tracker, silicon microstrip detectors were chosen as the baseline design for the following reasons:

1. The very fine segmentation possible combined with proven high radiation resistance make this detector ideal as the element closest (10 cm) to the interaction point.

2. Very high spatial resolution allows very precise vertex position and track impact parameter measurement.

3. It is a mature technology, which is presently in use in a number of fixed target and collider experiments with relatively well understood performance, radiation resistance and cost properties.

Silicon detectors were considered to be too expensive for the outer tracker. The Interpolating Pad Chambers were chosen for the baseline design.

The Silicon Microstrip inner tracker consists of six layers of silicon strip ladders. The geometrical layout of the silicon is shown in figure 29. Each ladder is composed of two back-to-back single sided silicon sensors with a 5 mrad stereo angle between the two sensors. Each sensor is 300 μm thick with a strip pitch of 50 μm. Each pair of sensors provides a space point with a resolution of 10 μm in the $r-\phi$ plane and 3 mm in the $r-z$ projection. The six layers of ladders are organized into three superlayers, each of which provides a track stub to a track finding algorithm. In the forward region, the silicon sensors are mounted into disks with the strips projecting radially inward toward the beam axis. The silicon tracker is 200 cm long and extends in a radius from 10 to 35 cm. The total area of silicon ladders in the detector is about 7 m^2 with about $3.2\text{x}10^6$ strips to be read out. The readout will be highly multiplexed, with 1028 strips to one fiber optic readout channel, for a total readout channel count of 3500.

The outer tracker consists of 8 layers of pad chambers, both in the barrel region at radii between 35 and 70 cm, and in the forward region which extends from 20 to 70 cm in radius. The 8 layers are arranged in 4 superlayers with 2 layers each. Each barrel layer will consist of 20 chambers, each covering 18° in azimuth, with the largest chamber being 30 cm wide x

200 cm long. The forward layers will be disks divided into ten trapezoidal chambers about 50 cm x 50 cm each.

4.3.2 Physics Goals, Design Parameters, and Detector Performance of the GEM Central Tracker

The physics goals for the central tracking in GEM can be divided into two categories. The first are those features that are required to support the primary objectives of GEM, namely the detection of gammas, electrons and muons at high p_T. Some examples of these are:

- Identify the primary vertex of an event of interest, so that it can be separated from other pileup events in the memory time of the detector.
- Separate electrons and gammas using the presence or absence of a charged track pointing to an electromagnetic shower in the calorimeter.
- Provide track information for e, μ or γ isolation cuts, and to help with rejection of conversions and Dalitz pairs.
- Help with electron-hadron separation by providing a momentum measurement that can be compared with the energy deposition in the calorimeter.
- Help with rejection of background by matching the muon momentum measured in the central tracker with the momentum measued in the muon chambers.
- Determine the electron sign up to 400 GeV/c.

The tracker should be able to fulfill these goals well at the design luminosity of $10^{33} cm^{-2} s^{-1}$. These capabilities should also survive to luminosities up to $10^{34} cm^{-2} s^{-1}$. These minumum goals do not require full pattern recognition, but can be met by looking for hits in the tracker in a specific road extrapolated from the calorimeter or the muon system.

The second category of physics goals are more ambitious:

- Full reconstruction of the charged tracks in the event.
- Secondary vertex finding.
- Tracking at low momenta with good resolution.

These features would enhance GEM's ability to address issues such as b and top physics. They are more demanding in that they require pattern recognition capabilities and very good vertex resolution. It is expected that these more ambitious goals can be met at luminosities up to $10^{33} cm^{-2} s^{-1}$, but probably not much higher. This, however, seems satisfactory since the physics topics requiring these more ambitious features have relatively large cross sections and can thus be studied at luminosities of $10^{33} cm^{-2} s^{-1}$ or below.

The design parameters for the central tracker that will satisfy the goals outlined above are summarized in Table 4 which follows.

Outer Radius	70 cm
Length	±150 cm
Rapidity Coverage	$\|\eta\| \leq 2.5$
Magnetic Field	0.8T
Occupancy	
at $\mathcal{L} = 10^{33} cm^{-2} sec^{-1}$	≤1%
at $\mathcal{L} = 10^{34} cm^{-2} sec^{-1}$	≤10%
Charge separation at 95% C.L.	$p \leq 400$ GeV/c
Momentum Resolution at 90°	
at high momenta	
(measurements limited)	$\Delta p/p^2 \sim 1.3 \times 10^{-3} (GeV/c)^{-1}$
at low momenta	
(multiple scattering limited)	$\Delta p/p \sim 4\%$
Vertex Resolution	
along beam direction	$\delta z \sim 1$mm
impact parameter	$\delta b \sim 30 \mu$m
	above 10 GeV/c

Table 4. Design Parameters for the Central Tracker

4.3.3 Summary of Oregon Research to Date on GEM Tracking

Since joining the GEM Central Tracking Group in February, 1992, the Oregon group has been converting its GEM efforts from development of a silicon preradiator prototype for GEM to the silicon microstrip tracker of GEM. The work on the preradiator is described in section 4.2.

The work during the first half of this past year has concentrated on:

- Optimization of the GEM tracker, including both the silicon and IPC subsystems. For example, we reanalyzed the required stereo angles to achieve the desired z resolution and found a larger angle was needed. The GEM Central Tracking Group subsequently adopted a larger IPC stereo angle, converting from 30 milliradians to 100 milliradians.
- Analysis of the strip length constraints of the silicon detector. Substantial simplicity in the mechanical design of the GEM silicon microstrip detector is possible if we can operate with 18 centimeter long microstrips. Electronics noise analysis and GEANT pulse height simulations have been done to understand the sensitivity of operational reliability to the strip length.
- Preparation of specifications of the microstrip detectors for GEM. In this work we have identified the strip resistance as a crucial parameter for optimization. Typical strip resistances of 50-100 Ω/cm are too large, creating large dispersions in the signals. We have established a goal of 10 Ω/cm and are working with three silicon detector manufacturers to try to achieve this goal. All three are building prototypes with a goal to significantly reduce the strip resistance. We expect to receive samples of each early in 1993.

5. E-815

Fermilab experiment E-815 was officially approved in July 1992. The Oregon group had joined the proposed experiment in early 1992. This followed a Fermilab PAC recommendation that the E-815 collaboration needed strengthening, after which the Oregon and Rochester groups joined. The first run is presently scheduled for Fall 1994. The following discussion summarizes the experiment and the physics prospects. In the Renewal Proposal we discuss the proposed activities for the Oregon group in E-815.

E-815 will study ν_μ-induced charged and neutral current interactions (CC and NC) at high energy. It is an outgrowth of the E744/E770 experiments at FNAL employing the CCFR (Chicago, Columbia, Fermilab, and Rochester) detector in the Fermilab NCenter beam line. The primary proton beam will be 900 GeV with an intensity of $1\text{–}2\times10^{13}$ protons per pulse. A pulse occurs every 60 seconds and results in $\approx$ 20 CC events for 10^{13} protons on target. Fermilab has approved a minimum of 10^{18} total protons on target. After detector acceptance and fiducial cuts, this corresponds to a minimum of 1.1×10^6 CC events and 0.19×10^6 NC events.

Except for a few relatively minor modifications, E-815 will use the existing CCFR detector

in Lab E at FNAL. However, two substantial new factors promise to give E-815 a substantial edge over previous high-energy νN experiments. First, the high-intensity 900 GeV primary proton beam will result in a substantial increase in useful events. The high energy also allows for a cleaner separation of NC and CC events, which improves the detection efficiency. Secondly, the target will be followed by new sign-selected quadrupole triplet (SSQT) optics. The SSQT allows the sign of charge of the secondary particles to be selected, hence resulting in a selection at the detector of ν_μ or $\bar{\nu}_\mu$. This gives a much improved understanding of systematic errors, resulting in lower total errors in the electroweak parameters, as discussed below.

The primary physics goals of E-815 are the measurements of the electroweak parameters $\sin^2\theta_W$ and ρ. After its initial run in 1994, E-815 will improve the error on $\sin^2\theta_W$ by a factor of 2–3 ($\delta\sin^2\theta_W \approx 0.003$) and will improve the ρ measurement by ≈ 4 ($\delta\rho \approx 0.007$). In fact, the present ρ measurements are based on only ≈ 2000 $\bar{\nu}_\mu$ NC events. The relationships between the electroweak parameters and the experimental observables can be illustrated with the quantities R^ν and $R^{\bar{\nu}}$ (other similar quantities can be more useful, depending upon the specific mix of input errors), which are related to ρ and $z = \sin^2\theta_W$ by:

$$R^\nu = \rho^2(\frac{1}{2} - z + \frac{5}{9}z^2(1+r))$$

$$R^{\bar{\nu}} = \rho^2(\frac{1}{2} - z + \frac{5}{9}z^2(1+\frac{1}{r}))\,,$$

where

$$R^\nu = \sigma^\nu_{NC}/\sigma^\nu_{CC}\,,$$

$$R^{\bar{\nu}} = \sigma^{\bar{\nu}}_{NC}/\sigma^{\bar{\nu}}_{CC}\,,$$

$$r = \sigma^{\bar{\nu}}_{CC}/\sigma^\nu_{CC}\,,$$

with σ_{CC} (σ_{NC}) the CC (NC) cross section.

Figure 30 shows how E-815 will substantially improve the errors in the $\sin^2\theta_W$-ρ plane. Central values of $\rho = 1.0032$ and $\sin^2\theta_W = 0.23$ are assumed. Also shown are the bands for the allowed regions based on the M_Z and M_W measurements. The slope of the M_Z band is due to radiative corrections, primarily from the top quark. If the M_Z band is limited by other measurements, this translates into a limit in the top-quark mass. E-815 would limit the top-quark mass to better than 20 GeV/c^2.

Contributions of the oblique radiative corrections to deviations from the Standard Model can be parameterized in terms of the S and T variables of Peskin and Takeuchi. For example, $m_t = 200$ GeV/c^2 gives $\Delta T = 0.7$, and Technicolor would give ΔS =0.4–2, depending on details. The experimental sensitivity of R^ν and $R^{\bar{\nu}}$ can be expressed in terms of S and T:

$$\delta R^\nu/R^\nu = -0.0078S + 0.0212T$$

$$\delta R^{\bar{\nu}}/R^{\bar{\nu}} = 0.0003S + 0.0154T\,.$$

Figure 31 uses these relations to show the expected E-815 errors in the $S - T$ plane. The line at $S = .0$ is the Standard Model for different values of the top-quark mass, where $T = 0$ corresponds to $m_t = 140$ GeV/c^2.

As can be seen from these figures, E-815 is competitive with LEP/SLC and CDF/D0 in the magnitude of benchmark errors. And because its connection to the Standard Model relations and its systematics are unique, it will provide an additional valuable probe of the Standard Model. In fact, if the Fermilab νN program is continued through the 1990's with an upgrade to the detector and expected improvements to the beam, the CC and NC measurements will continue to be competitive. In the table below, "Phase I" refers to the situation of the mid-1990's, with νN errors from E-815. "Phase II" refers to the late 1990's with upgraded detector and beam. Figures 32 and 33 indicate how the errors would change in the Phase II scenario. The expected improvements resulting from other measurements have been included. The band for A_{LR} assuming $\delta A_{LR} = 0.004$ is probably overly optimistic: The value of $\delta A_{LR} = 0.007$ corresponds to 1.5×10^5 Z events at SLC with 60% polarization, which may be a more realistic expectation. To indicate sensitity to physics beyond the Standard Model, Fig. 32 shows the shift in S of the Standard Model line due to one Technicolor generation. In fact, νN is quite sensitive to many types of new physics, for example a heavy top quark, a non-standard Higgs sector, or new heavy gauge bosons (Z'). The details for quantifying these sensitivities can be found in reference [17]

Quantity	Error Current	Error Phase I	Error Phase II
R^{ν}	1.4%	0.82%	0.33%
$R^{\bar{\nu}}$	4.5%	1.41%	0.51%
M_W	310 MeV	100 MeV	70 MeV
Γ_Z	26 MeV	15 MeV	15 MeV
A_{LR}	—	.0007	.0004
Q_W	1.80	0.60	0.40

Table 5. Sensitivity of Various Electroweak Measurements

Besides the electroweak measurements, there are a number of other interesting physics topics in E-815. We briefly mention some of these. The QCD parameter Λ_{QCD} is best determined in νN. A "Phase II" measurement could push the uncertainty in Λ_{QCD} to 15 MeV. Structure function measurements will still be interesting, and many of these measurements will have to be made anyway to produce the electroweak results (e.g., the contribution of the strange

sea). The limits on $\nu_\mu \rightarrow \nu_e$ oscillations can be extended. (The possibilty of doing a $\nu_\mu \rightarrow \nu_\tau$ measurement is under study.) Wrong-sign single muon events and dimuon events, when compared to predictions, provide direct probes of rare phenomema (e.g. lepton number violation). Especially for neutrino phenomena, the large number of events in E-815 will be equivalent (given kinematic constraints) to $\sim 10^6$ neutrino events at LEP.

The major new beam optics for E-815 is the sign-selected quadrupole triplet (SSQT), which as stated at the begining, will select the charge of the secondaries. The resulting separation of ν_μ and $\bar{\nu}_\mu$ events allows for a clean measurement of R^ν and $R^{\bar{\nu}}$ (or related quantities). An additional important aspect of the SSQT is in reducing the systematic uncertainty due to the ν_e background. ν_e-induced events are difficult to distinguish from the ν_μ NC signal. The error associated with modelling this background was the most significant measurement error in $\sin^2\theta_W$ in E744/E770. With the SSQT beam, the $K^0_L \rightarrow \pi^- e^+ \nu_e$ events are completely removed. The remaining ν_e contribution from $K^+ \rightarrow \pi^0 e^+ \nu_e$ can be measured from the CC data (to get the K^+ flux) and the known branching ratios.

6. TAU-CHARM FACTORY

In 1989 the Oregon group became a member of a U.S. tau-charm factory (τcF) collaboration. A brief history and present status follow. The expected approval of this project for a Spanish site during 1991-92 did not come about. The Oregon activities have been, for the most part, put on hold during the past year. The exception to this was some interesting detector development work, including a beam test at TRIUMF, Vancouver, B.C. The Oregon group actively participated in this effort, which is briefly described after the history.

Discussions of a high luminosity e^+e^- collider operating in the 3–4.2 GeV energy range and a luminosity of $\approx 10^{33}$ cm^{-2}s^{-1}were initiated by Kirkby [18] and Jowett [19]. A workshop was held at SLAC in May, 1989 which helped define the project.[20] An accelerator study of the technical feasibility of a τcF was performed by the U.S. group. In 1990 the site effort shifted to Europe. Spain requested advice from CERN on the technical merits of a τcF. The response[21] was delivered to the Spanish government in November 1990. This report endorsed the technical feasibilty of the τcF and laid out a budget and schedule, calling for completion in 5 years at a cost of 300 MSF for accelerator and laboratory, and 90 MSF for the detector. In February, 1991, the Spanish government indicated to CERN that they would provide the funding for the project at a Spanish site. Spain solidified its committment to the τcF by hosting a workshop at the University of Sevilla April 29 - May 2, 1991. Approximately 100 participants took part in physics, detector, and accelerator design discussions. Spain would call on other laboratories, primarily CERN, to provide the necessary technical expertise to build the accelerator. The τcF has been ratified by the CERN scientific policy committee but has not been approved by the CERN Council. An agreement of terms between CERN and Spain has not been forthcoming.

The U.S. τcF group consists of physicists from SLAC and the Universities of Cincinnati, Illinois, Oregon, Washington, the University of California at Santa Cruz, MIT, Rutgers, and the University of Texas at Dallas.

The TRIUMF beam test took place in August 1992. The primary goal was to measure the properties of CsI blocks of various types and from different manufacturers, to test the custom readout electronics, and to examine some engineering options for crystal mounting, electronics cooling, etc. The test was very successful. Analysis is ongoing, but some initial results from the CsI response are given below.

In addition, the Oregon group brought to TRIUMF a set of silicon strip detectors with custom analog electronics for readout. The idea is that if a high-granularity detector could be inserted into the CsI near electromagnetic shower maximum, then the position of photons could be determined more readily than with the CsI (weighted mean) position alone. Since the CsI crystals were to be separated longitudinally in any case (mainly for background suppression), this seemed to be a natural avenue of pursuit. Unfortunately, as was brought out at the Sevilla meeting [22] , the main problem with this scheme is that according to EGS simulations, the low-energy (< 150 MeV) photons do not produce many charged particles in their showers, hence producing large fluctuations in the silicon measurement. And it is at these low energies that the photon position determined by the CsI alone needs the most help. Therefore, the goal of the silicon strip test at TRIUMF was to determine if the EGS simulations were correct. Data was taken at TRIUMF with the strips placed between longitudinal sections of the CsI ($\approx 3X_0$ from the front face). This data has not yet been analyzed.

Data was taken in the M11 and M13 beam lines at TRIUMF. The beam momentum ranged from 40 to 400 MeV/c. CsI crystals of transverse dimension ranging from 4 cm to 8 cm were were stacked together in arrays which were, on average, four crystal blocks on a side. Each crystal was readout by wavelength shifter bars with 4 photodiodes. The photodiodes were fed into low-noise preamplifiers built at SLAC, followed by LRS 2249A ADCs. A low-mass drift chamber built by the Washington group provided the positions and angles of the incoming beam particles. Particle identification was accomplished using time of flight. Beam conditions and rates were generally quite good, allowing for a number of different configurations to be thoroughly tested over a range of energies.

Figures 34 and 35 are the time of flight distributions at $p = 150$ MeV/c and 300 MeV/c, respectively. The following plots are for the $p = 300$ MeV/c running, where a selection has been made to enhance electrons by demanding $time(TOF) > 368$ (see Fig. 34, where the TOF unit is TDC counts). For this run the beam was centered on a 6.4 cm $\times$6.4 cm $\times$ $16X_0$ CsI(Tl) crystal, longitudinally segmented at $3X_0$ from the front face. Figs. 36 and 37 give the measured energy in the front and back crystals, respectively. Fig. 37 is the sum of the two. The resolution determined from the width of the electron peak is $\approx$6.5%. This is about twice what is expected, but is reasonable considering that this came directly from the online data with no front/back calibration and with losses beyond the center crystal.

7. Personnel

The participants of this research in 1992-93 were:

Faculty

James E. Brau

Raymond E. Frey

David Strom

Visiting Faculty

Anatoli Arodzero, Moscow State University

George Bashindzhagyan, Moscow State University

Postdoctoral Associates

Koichiro Furuno

Jennifer Huber

Engineering Staff

R.T. Kollipara

Students

Hyun Hwang

Matt Langston

Hwanbae Park

Kevin Pitts

Xiaoqing Yang

Jingchen Zhou

David Mason (undergraduate)

8. List of Publications

Please see vita at end of proposal.

9. Foreign Trips

Jim Brau - September 28, 1992 to October 3, 1992, Hamamatsu Company, Tohoku University, and Niigata University, Japan.

Jim Brau - October 4, 1992 to October 8, 1992, Industrial Technology Research Institute, Taiwan.

David Strom - March 26, 1991 to April 6, 1991, CERN, Luminosity monitor construction.

David Strom - May 28, 1992 to July 2, 1992, CERN, Luminosity monitor construction and test beam.

David Strom - July 29, 1992 to September 2, 1992, CERN, Luminosity monitor construction and test beam.

10. References

1. Hammamatsu Photonics K.K., Solid State Division, Hamamatsu City, Japan.
2. S.C. Berridge et al., IEEE Tans. Nucl. Sci. NS-37, 1191 (1990).
3. R. Brun et al., CERN-DD/78/2 (1978).
4. G. Haller et al., IEEE Trans. Nucl. Sci., NS-36 675 (1988).
5. E. Vella et al., IEEE Trans. Nucl. Scil, NS-36 822 (1988).
6. L. Einsweiler et al., IEEE Trans. Nucl. Sci., NS-35 316 (1988).
7. F.A. Berends et al., Nucl. Phys. B304 712 (1988).
8. OPAL Collaboration, "Proposal for Upgrading the OPAL Luminosity Detector," CERN/LEPC 91-9.
9. S. Jadach et al., "Higher Order QED Corrections to Bhabha Scattering at Low Angles," Phys. Lett. 260 (1991) 438.
10. F. Lemeilleur, et al., "The local Hardening Effect on Electromagnetic Showers," Phys. Lett. 222 (1989) 518.
11. R.Y. Zhu, "Signal and Background of $H \rightarrow \gamma\gamma$ with Proposed GEM Calorimeter Systems," Internal GEM Report, November 5, 1991.
12. Report of the 1990 HEPAP Subpanel on SSC Physics, DOE/ER-0434 (1990).
13. M.S. Chanowitz, "Electroweak Symmetry Breaking at the pp Colliders of the 1990's and Beyond," LBL-26613-MC (1989), Annu. Rev. Nucl. Part. Sci. 38, 323 (1988).
14. W. Marciano, Phys. Rev. Lett. 62, 2793 (1989); W. Bardeen, C.T. Hill and M. Linder, Fermilab-Pub-89/127-T; D.E. Kahana and S.H. Kahana, BNL-44380 (1990).
15. R.A. Todd et al., "Bipolar and CMOS ASIC Design for Large Physics Experiments," Proc. of the conference on Electronics for Future Colliders, p193, LeCroy Corp.
16. R. Barber et al., "The GEM Central Tracker, A Progress Report," March, 1992.
17. P. Langacker, M.X. Luo, and A.K. Mann, Rev. of Mod. Phys. **64**, 87, (1992).
18. J. Kirkby, "Discussions of a high luminosity e^+e^- Collider Operating," CERN-EP-87-210 (1987).
19. J. Jowett, CERN-LEP-87-56 (1987).
20. B. Barish, et al., SLAC-PUB-5180 (1990).
21. Y. Baconnier, et al., "A Tau-charm Factory Laboratory in Spain...," CERN/AC/90-07 (1990).
22. R. Frey, et al., "Proc. of the Meeting on the Tau-Charm Factory Detector and Machine," in press at CERN.

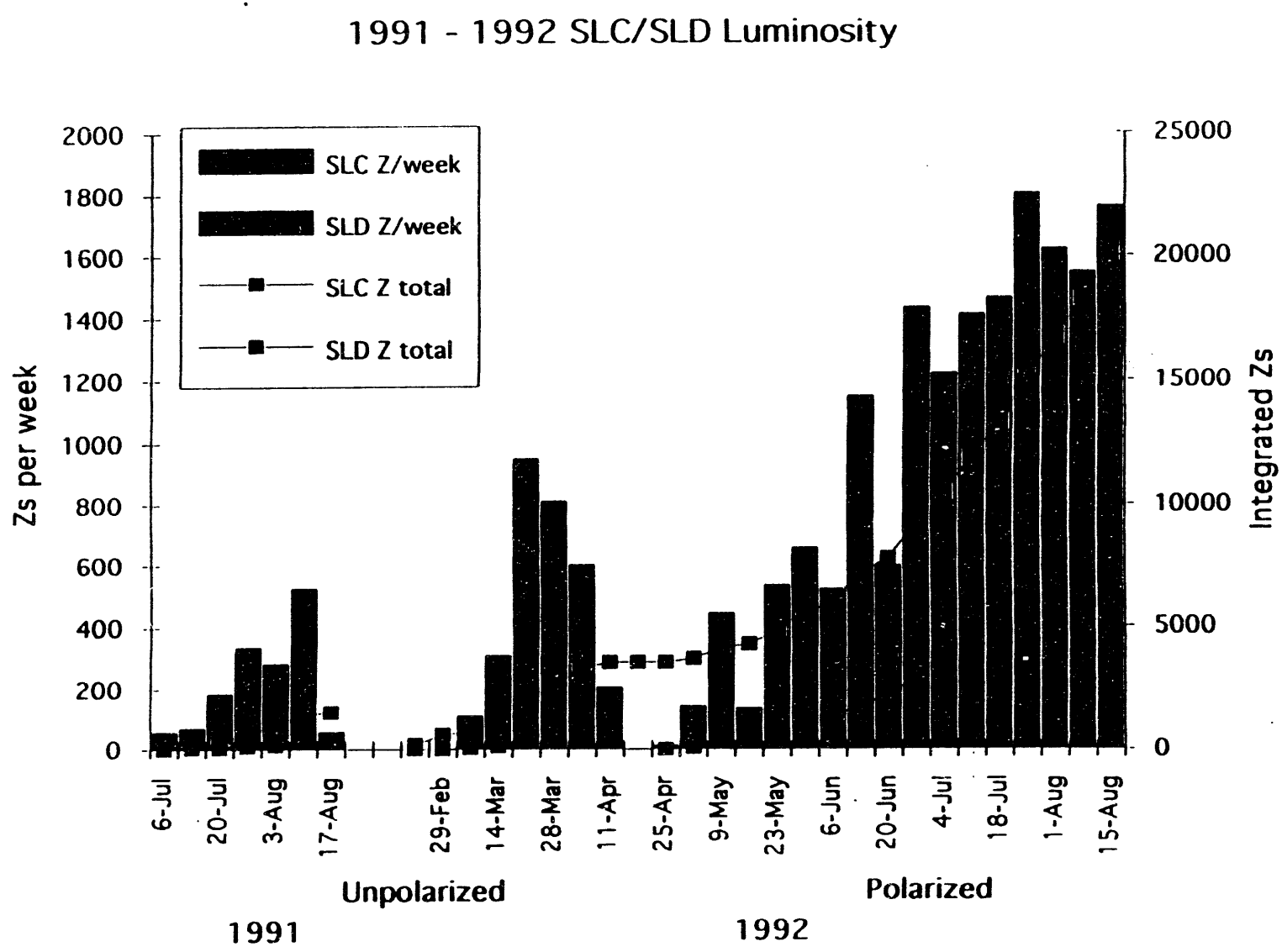
1991 - 1992 SLC/SLD Luminosity
SLC Z/week
SLD Z/week
SLC Z total
SLD Z total
Zs per week
Integrated Zs
2000
1800
1600
1400
1200
1000
800
600
400
200
0
25000
20000
15000
10000
5000
0
6-Jul
20-Jul
3-Aug
17-Aug
29-Feb
14-Mar
28-Mar
11-Apr
25-Apr
9-May
23-May
6-Jun
20-Jun
4-Jul
18-Jul
1-Aug
15-Aug
Unpolarized
Polarized
1991
1992

Figure 1

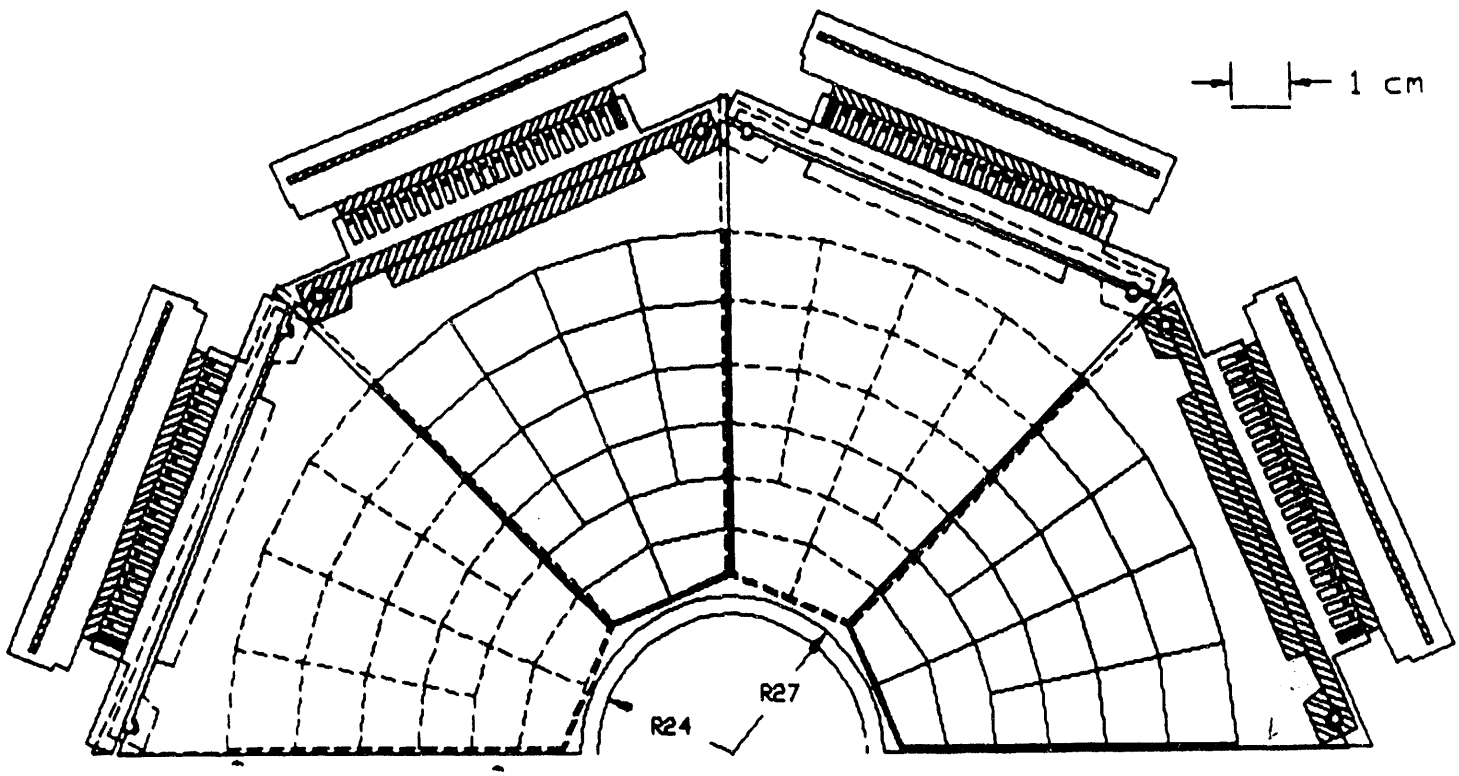

Figure 2
Front face of one LMSAT module as seen from the IP. Detectors shown with dashed lines have their ground planes facing away from the IP.

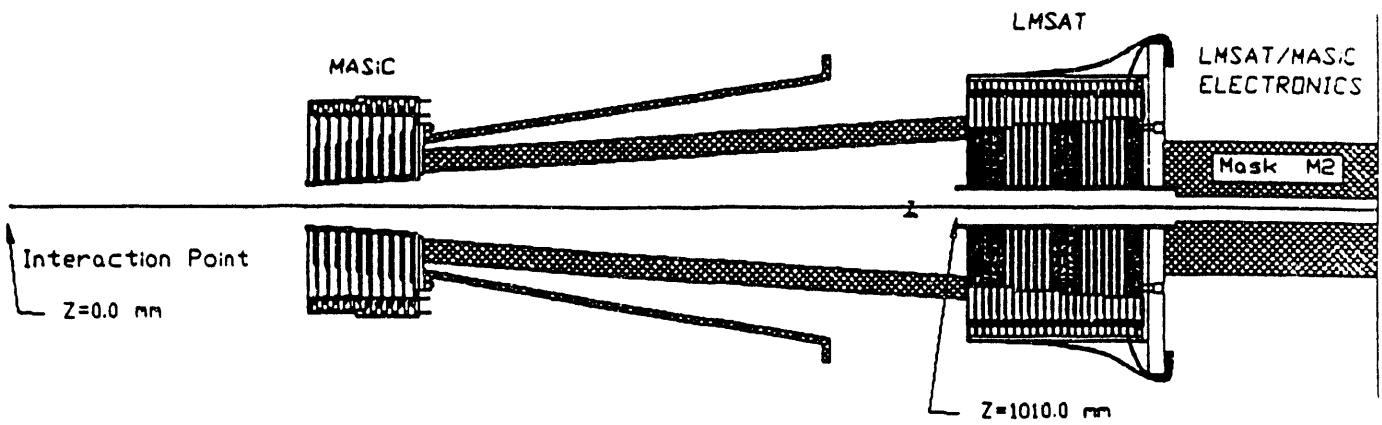

Figure 3
Side view showing LMSAT and MASC positions with respect to the IP.

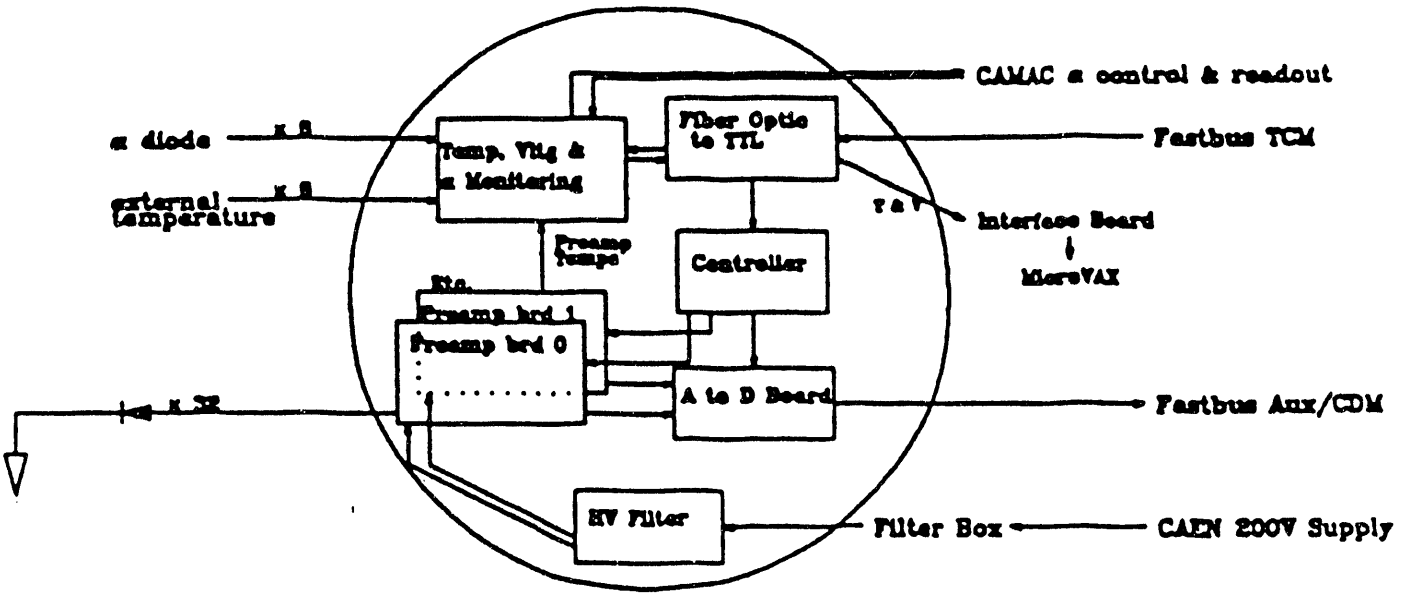

Figure 4
Block diagram of the LMSAT/MASC electronics.

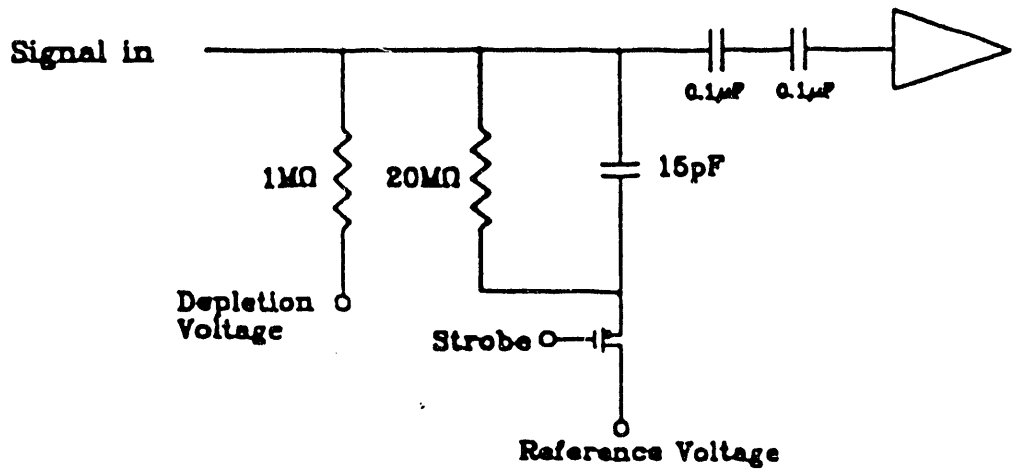

Figure 5
Leakage current measurement circuit.

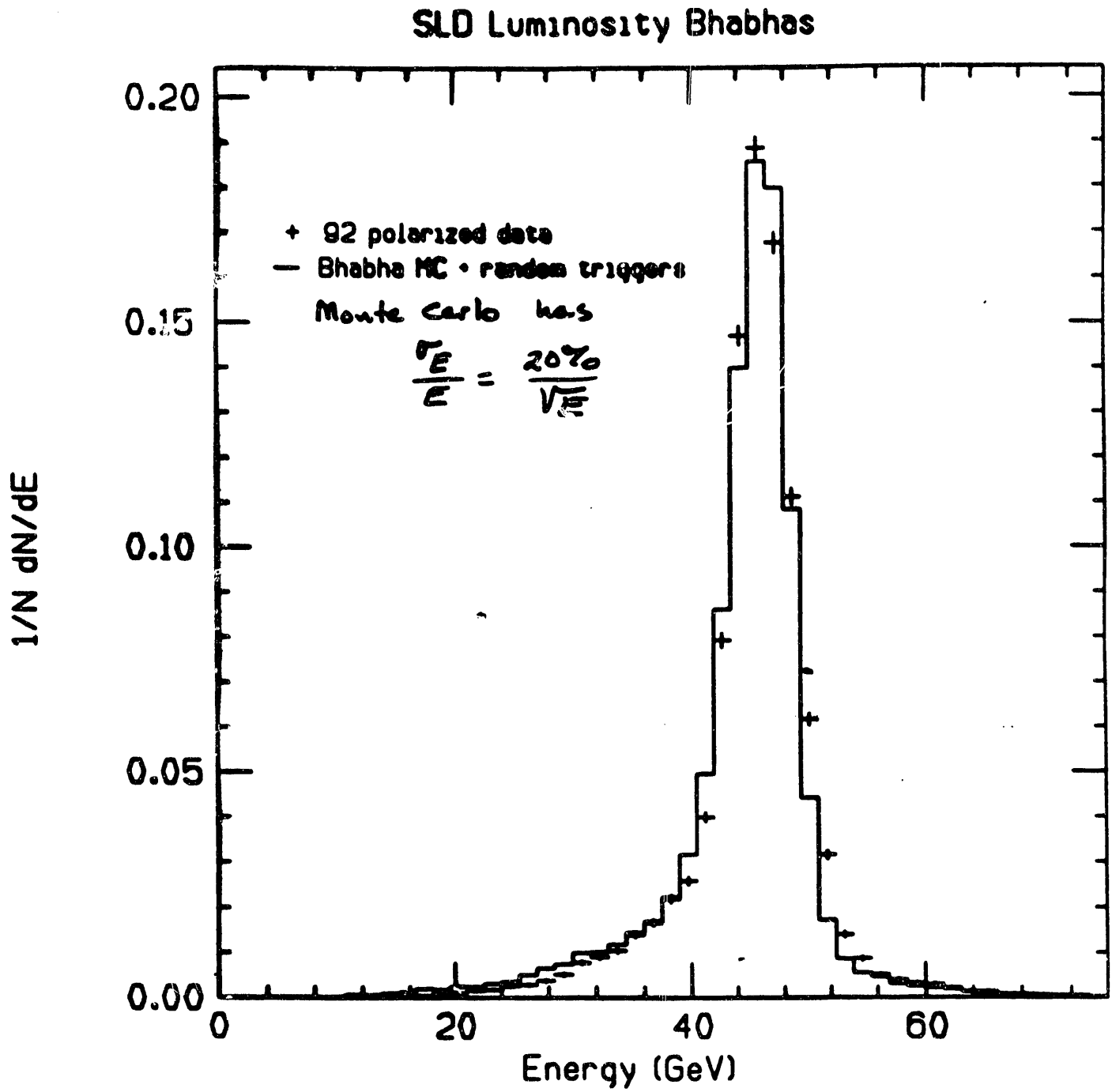

Figure 6
Energy distributions for data (points with error bars) and Monte Carlo (histogram).

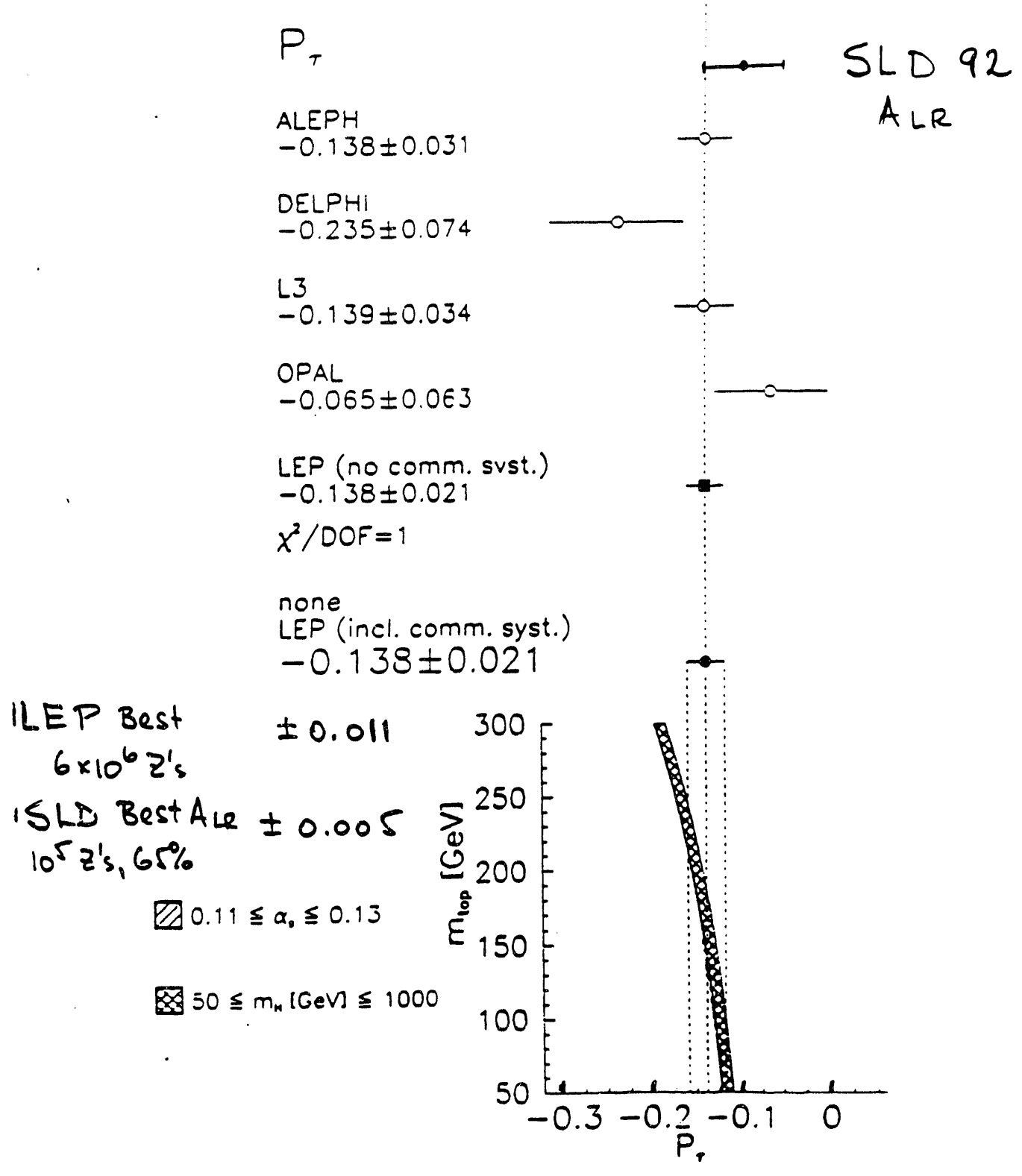

Figure 7
Comparison of LEP τ polarization measurements with the 1992 SLD A_{AR} measurement (preliminary).

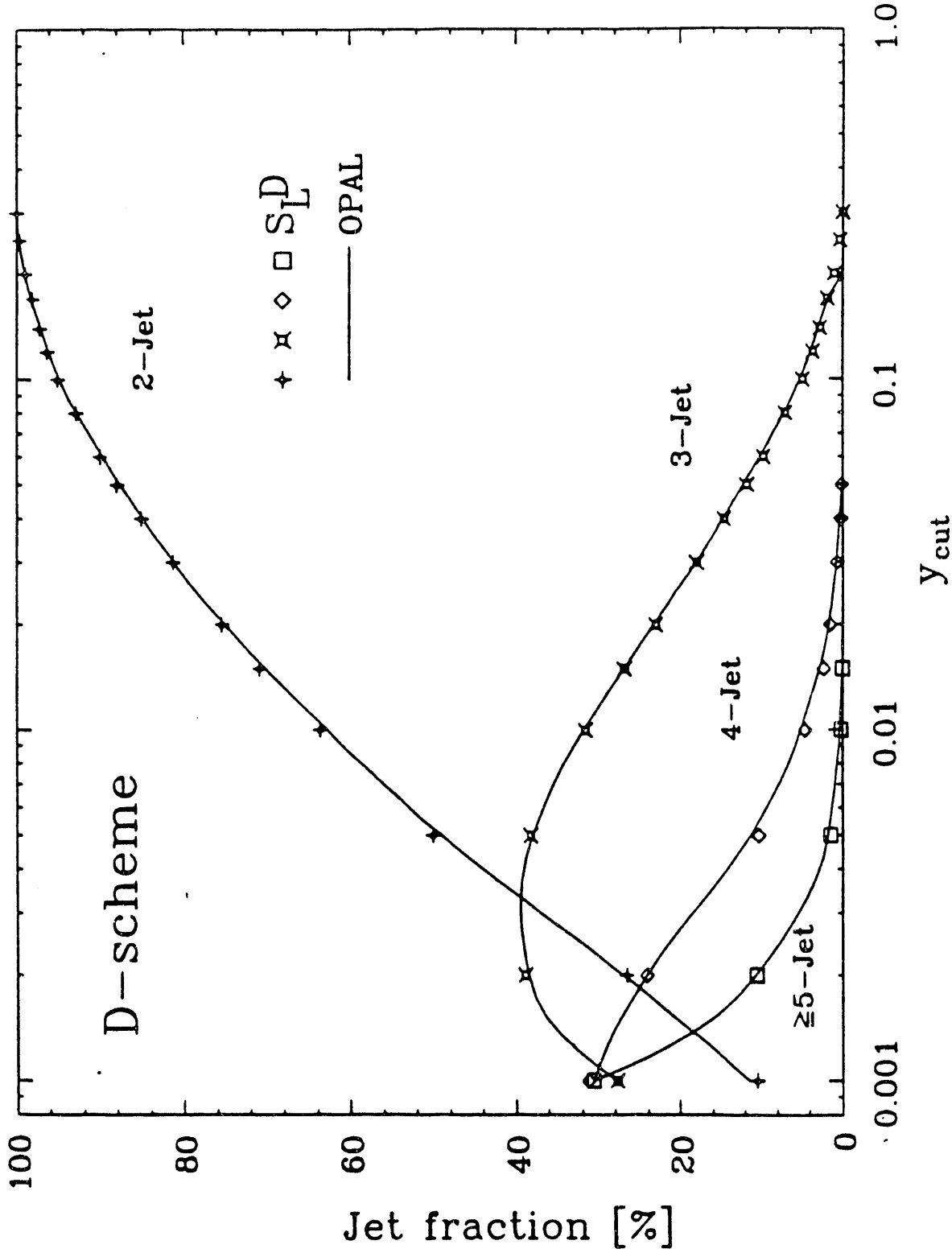

Figure 8
SLD Corrected Jet Rates

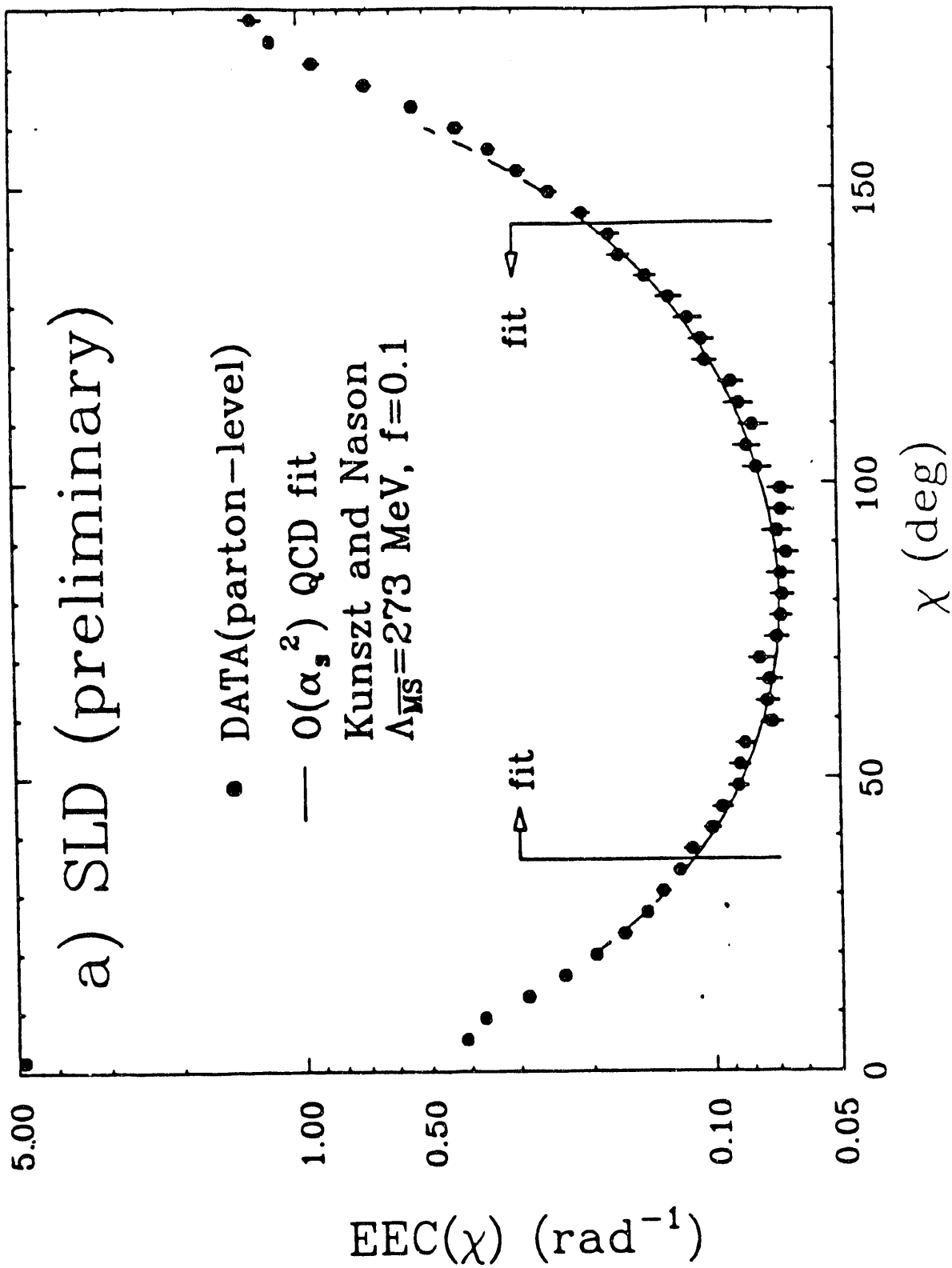

Figure 9
Fit of $O(\alpha_s^2)$ QCD Prediction

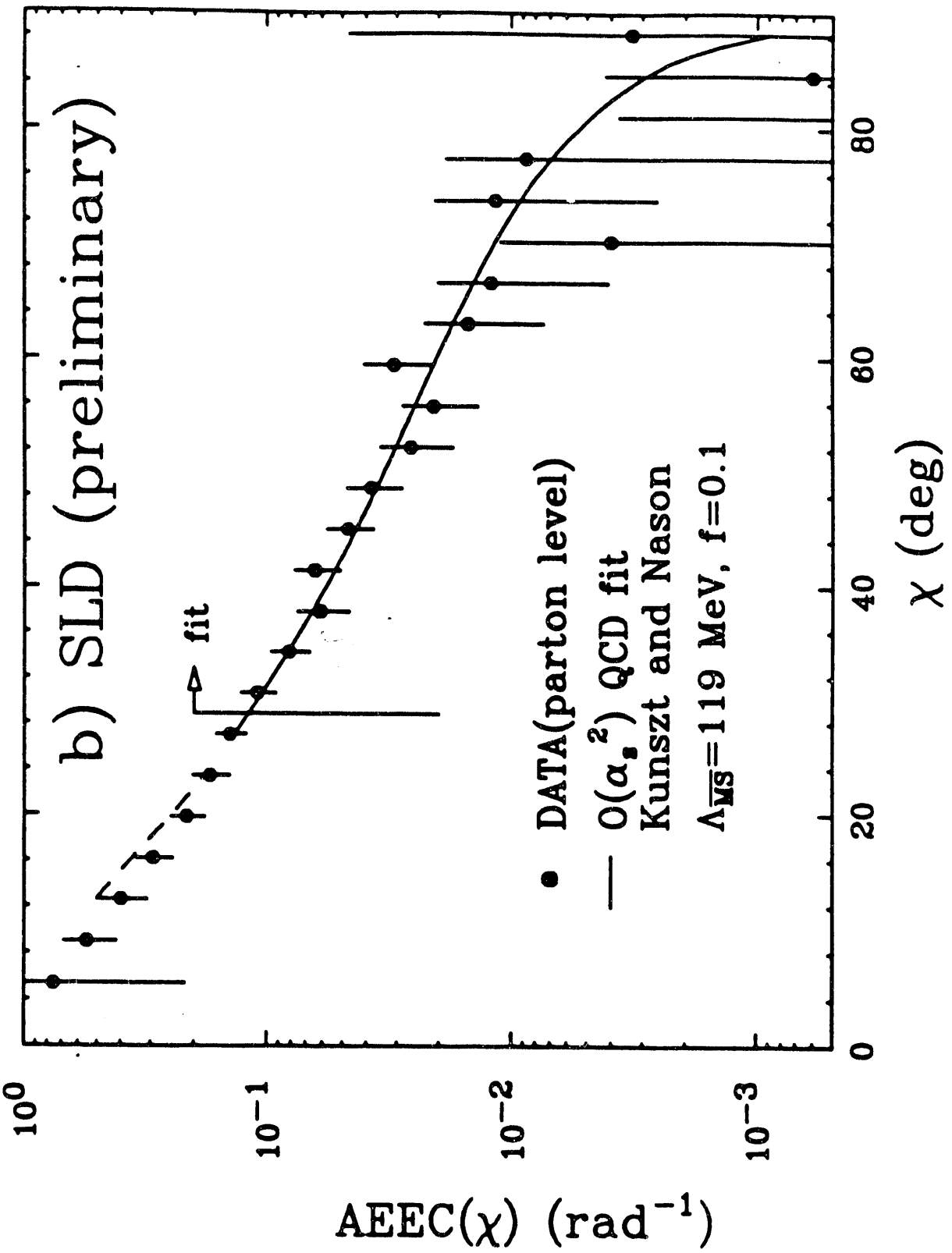

Figure 10
Asymmetry: EEC (π-x) - EEC(x)

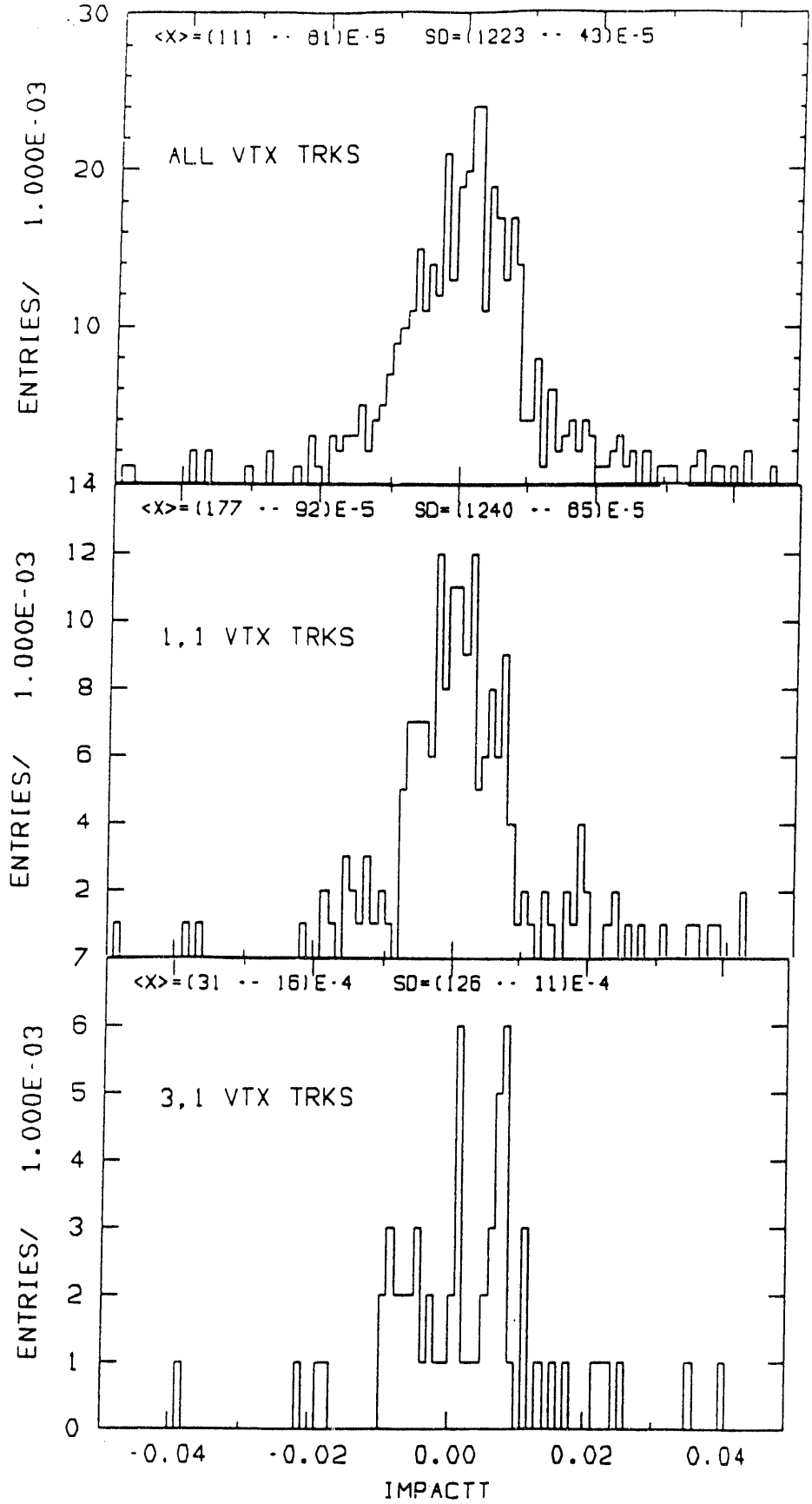
<X>=(111 -- 81)E-5 SD=(1223 -- 43)E-5
ALL VTX TRKS
ENTRIES/ 1.000E-03
30
20
10
14
<X>=(177 -- 92)E-5 SD=(1240 -- 85)E-5
1,1 VTX TRKS
ENTRIES/ 1.000E-03
12
10
8
6
4
2
7
<X>=(31 -- 16)E-4 SD=(126 -- 11)E-4
3,1 VTX TRKS
ENTRIES/ 1.000E-03
6
5
4
3
2
1
0
-0.04
-0.02
0.00
0.02
0.04
IMPACTT

Figure 11

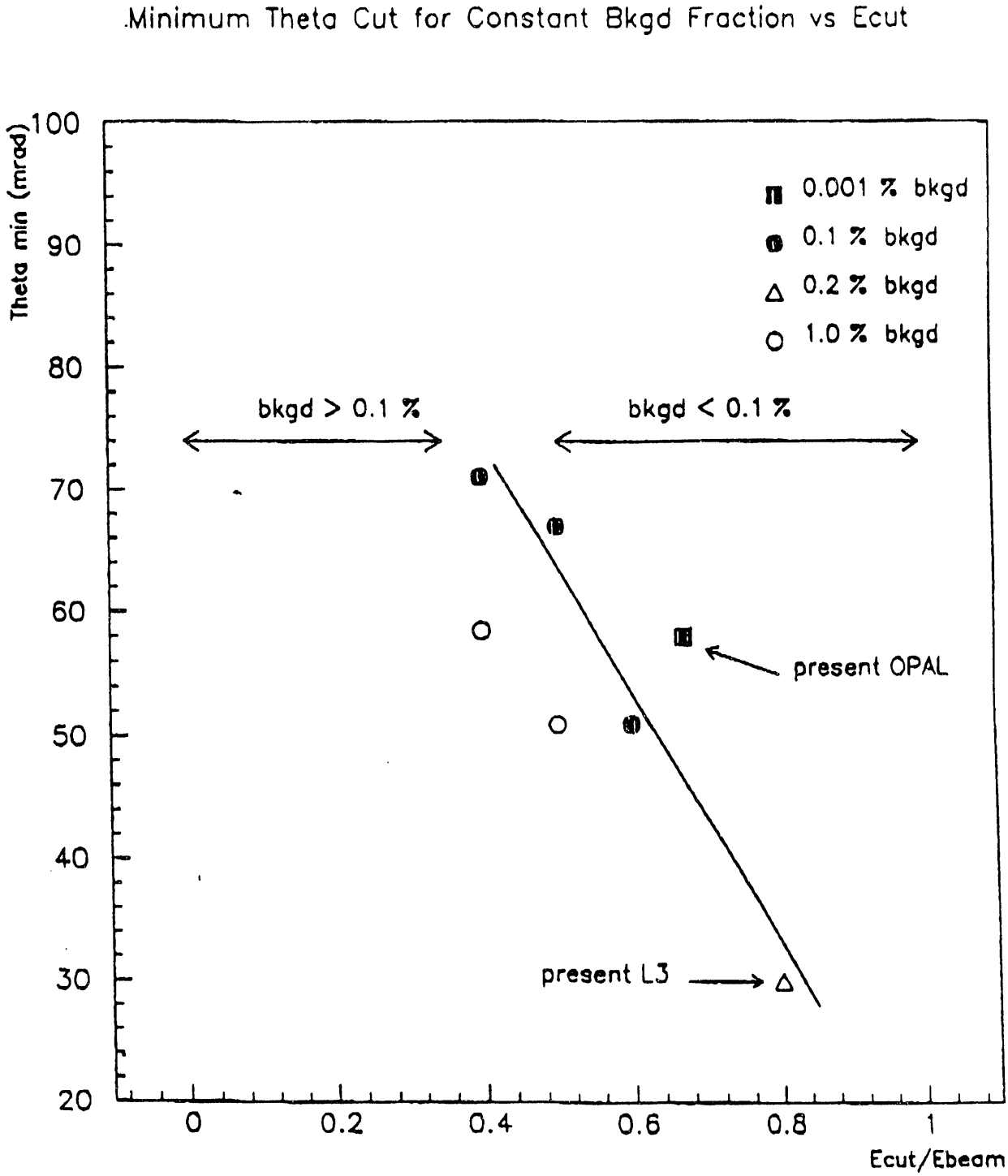

Figure 12
The background fraction as a function of the energy cut used to select background. Note that the background increases at higher energy cuts and smaller angles as expected.

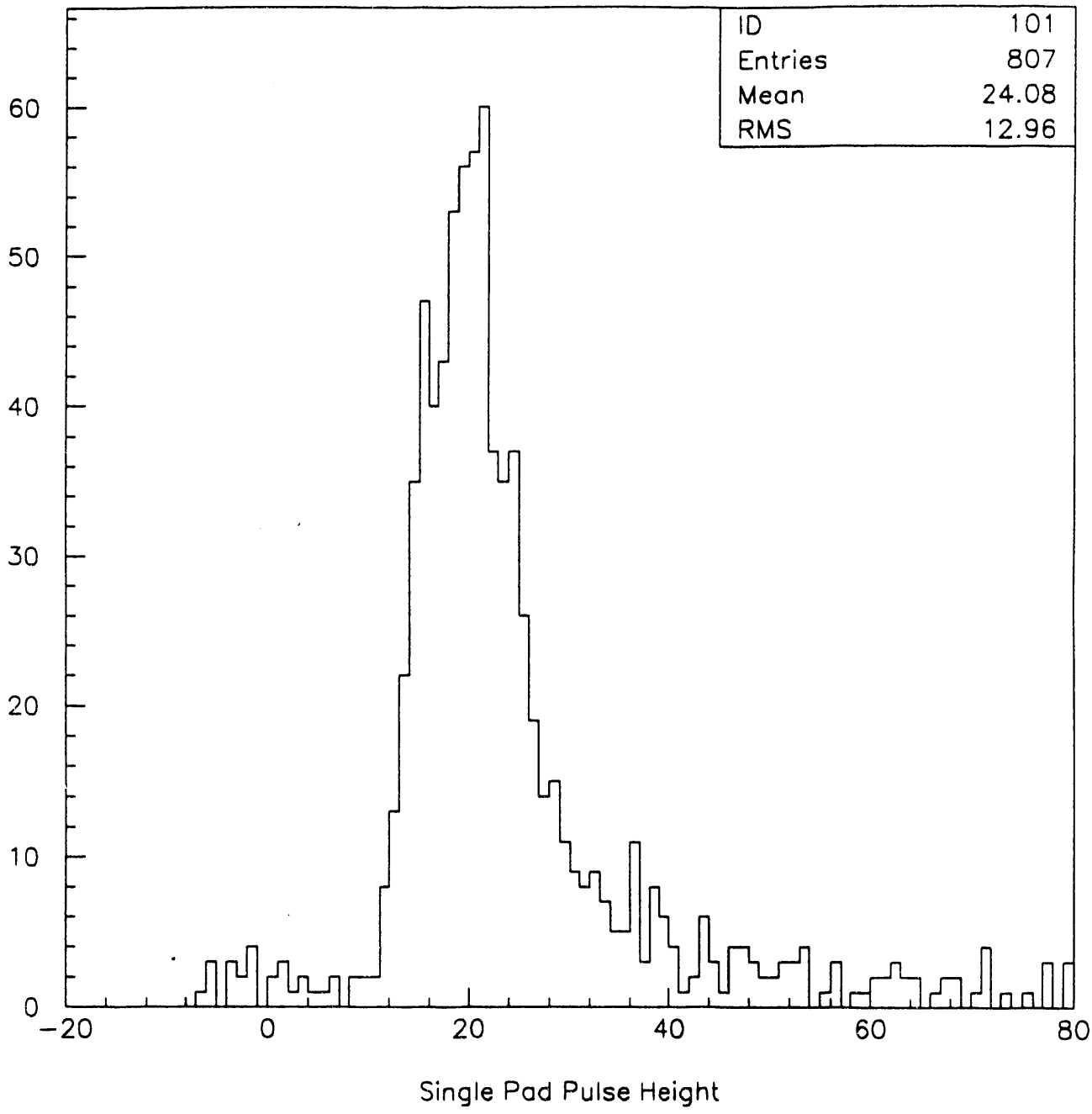

Figure 13
Typical energy spectrum from a single pad for a muon beam. The noise peak corresponds to those muons which have not traversed this particular pad.

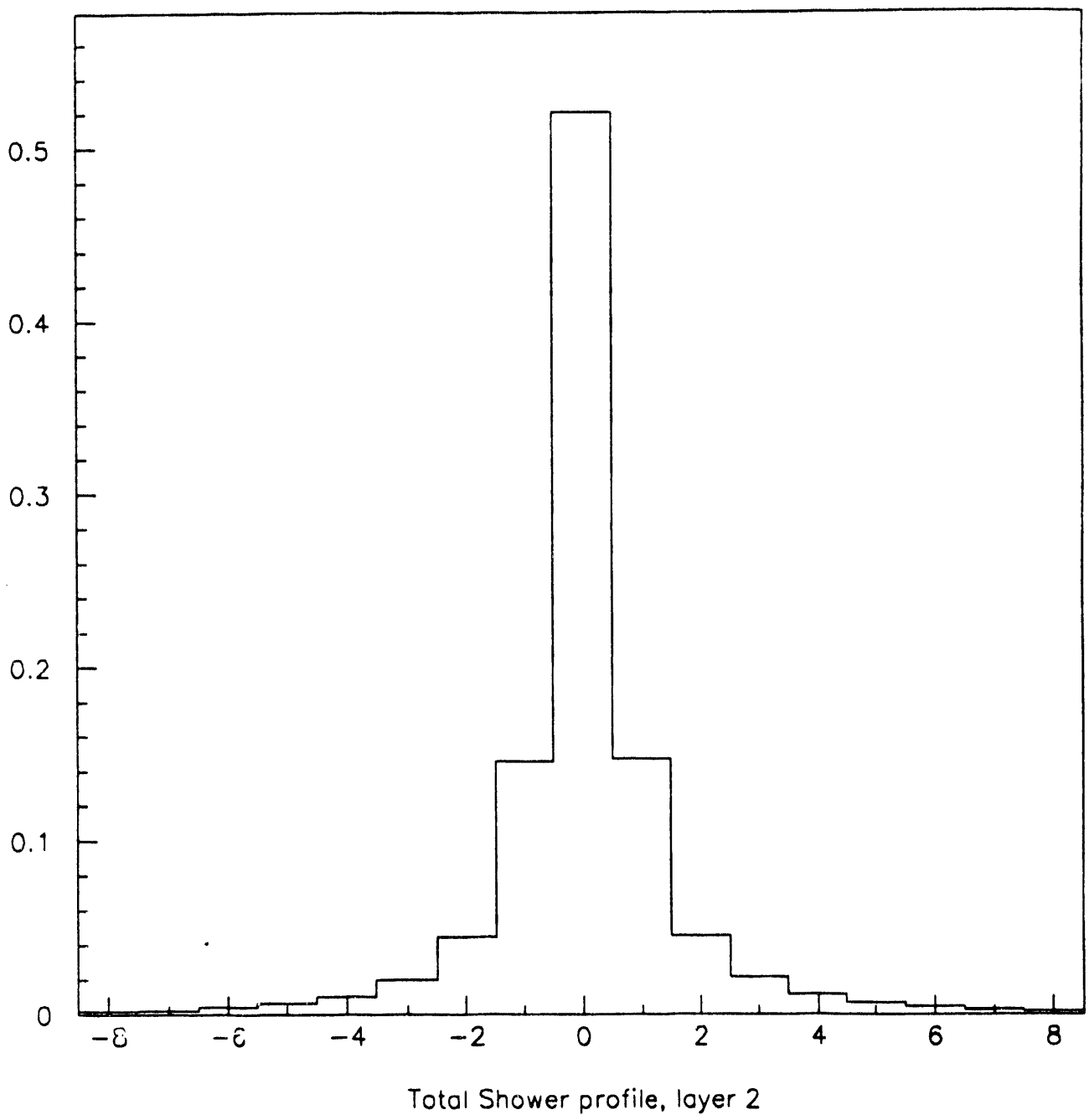

Figure 14
Average shower profile for showers seen at four radiation lengths as a function of pad number. The pads are 2.5 mm wide.

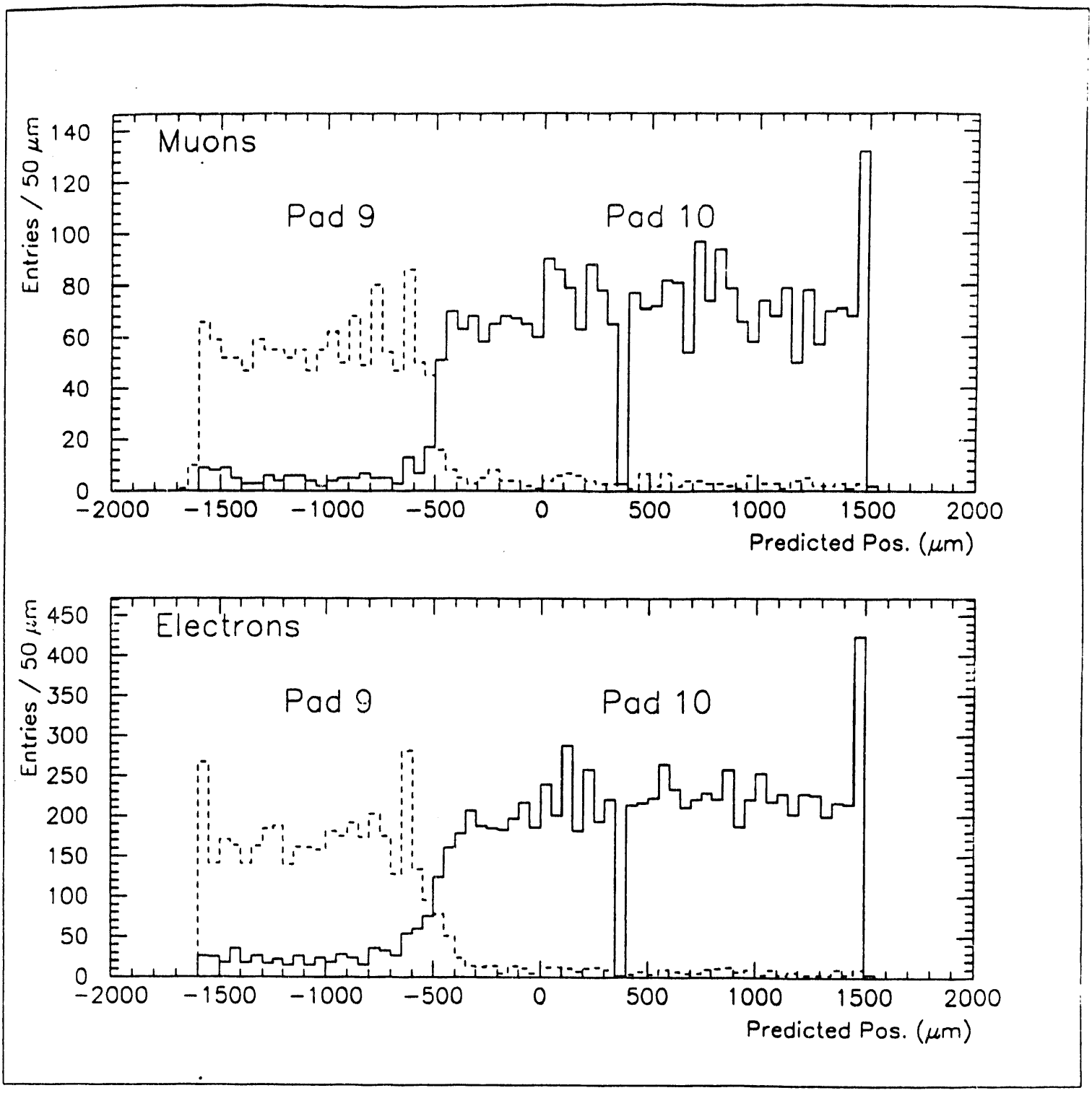

Figure 15

The number of events hitting a given pad as a function of the predicted position from the beam chambers and the microstrips. Note that the resolution for muons at the pad boundary is much better than the 50μm pitch of the microstrip detector. The same result is also shown for electrons. The pads shown were located at four radiation lengths.

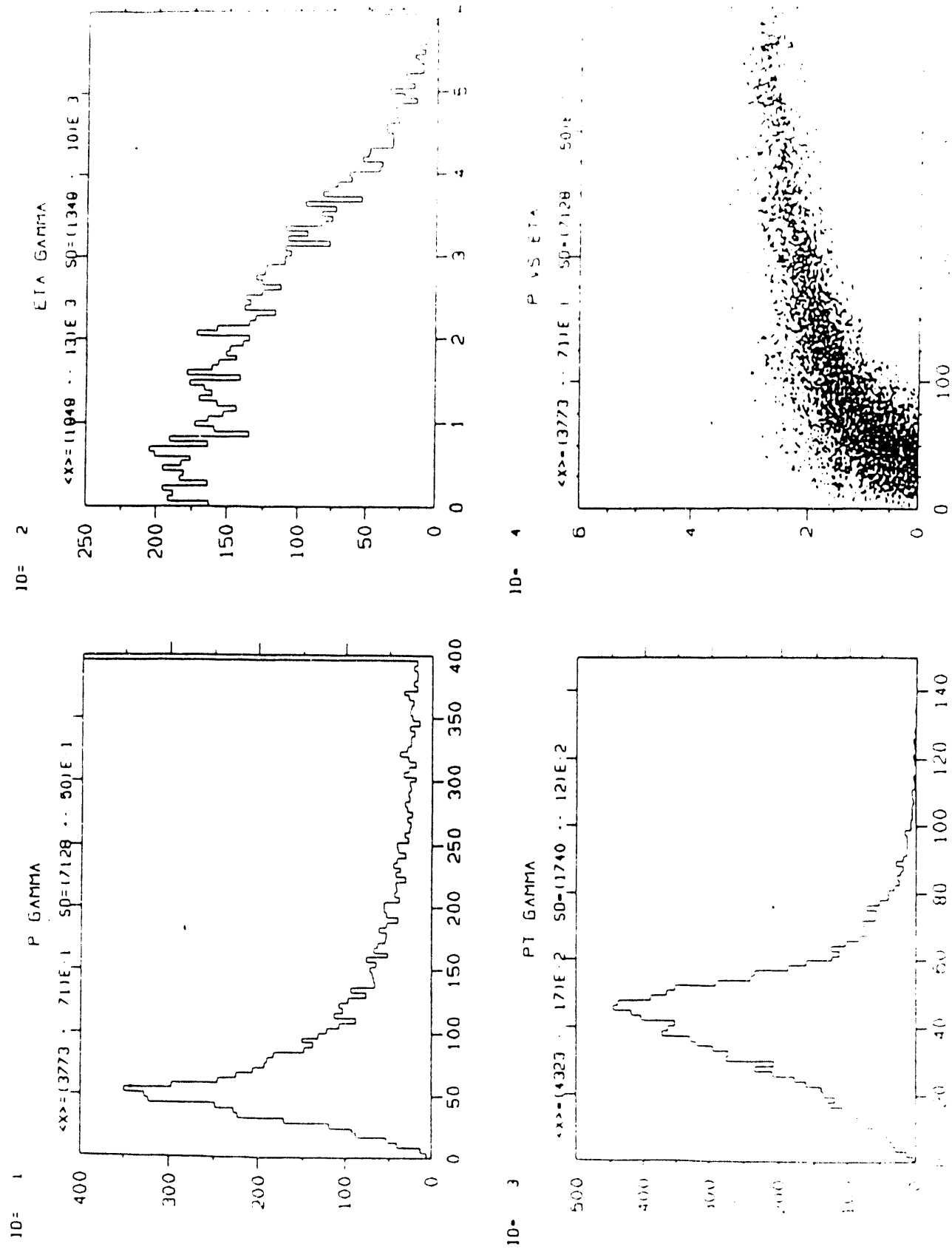

Figure 16

Distributions in the $H \rightarrow \gamma\gamma$ process for a 100 GeV Higgs. These plots show the γ energies, the γ pseudorapidities, the γ transverse momenta, and the correlation of γ energy with pseudorapidity. We note that a cutoff in pseudorapidity at 2.5 truncates the high end of the energy distribution.

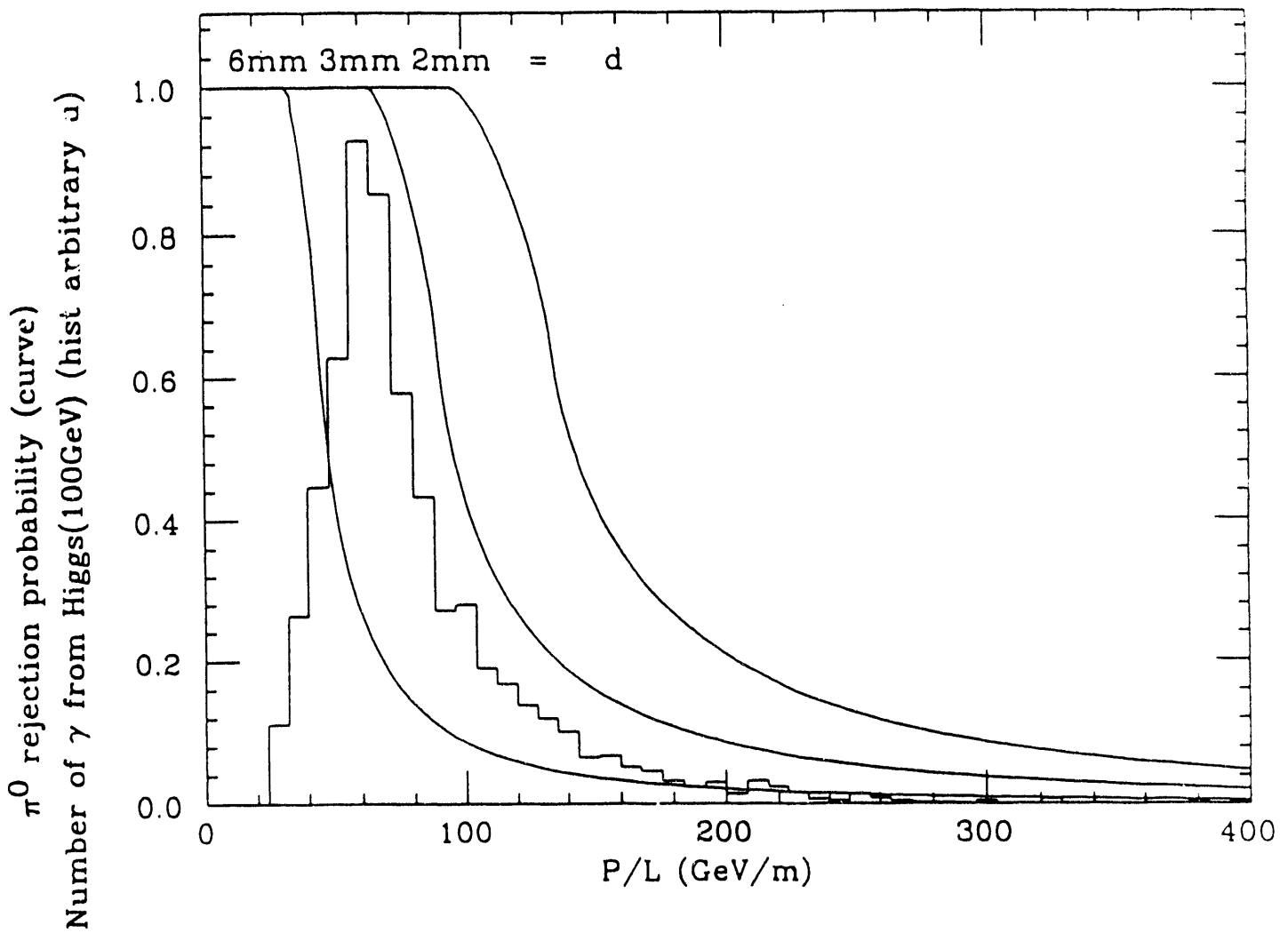

Figure 17

The optimal rejection power of a preradiator that requires separation of the two photons by 2, 3, or 6 mm in x or y as a function of the π^0 momentum divided by the pathlength from the

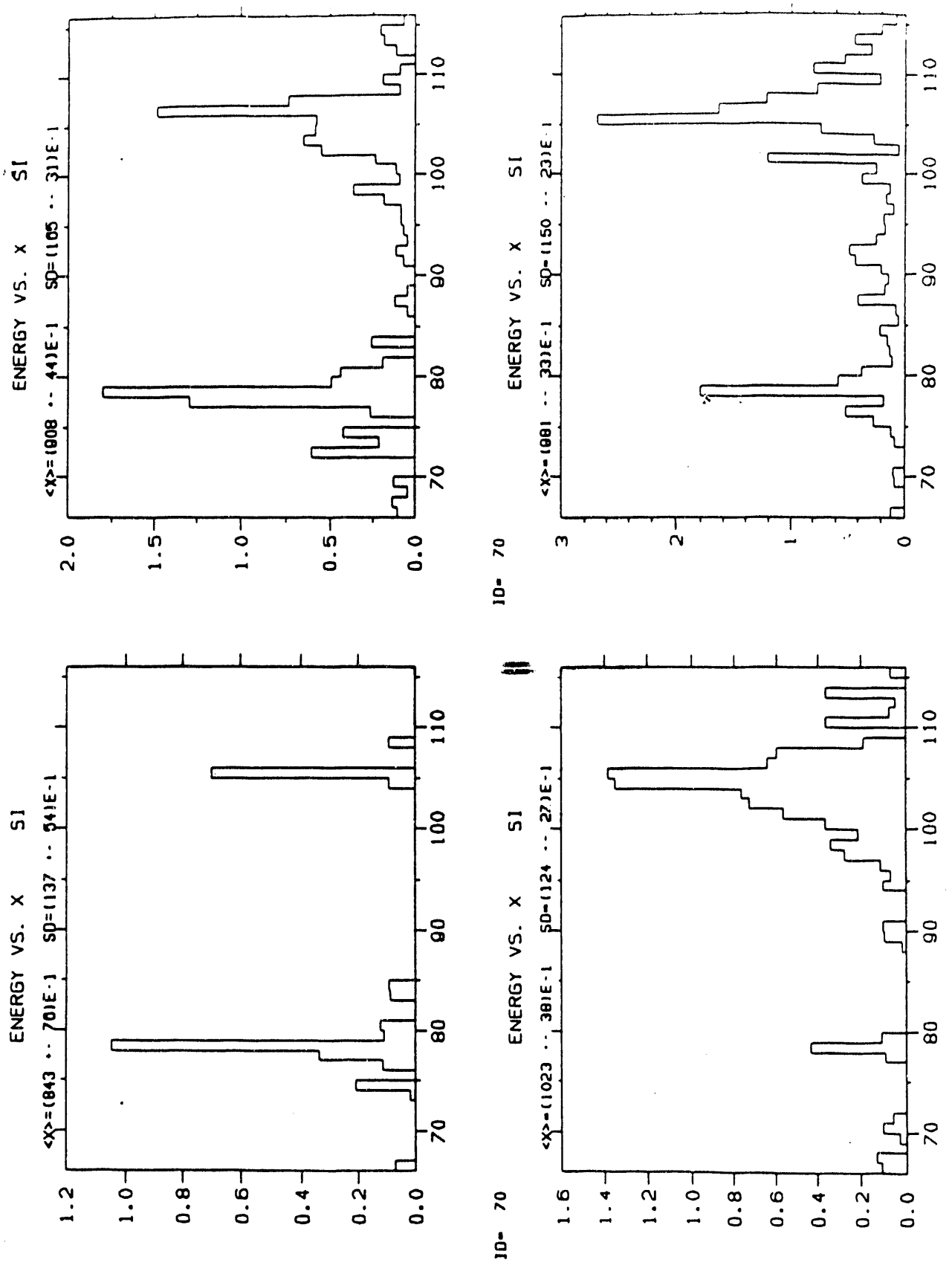

Figure 18
The pulseheight profiles in MeV for 50 GeV π^0s decaying with the minimal opening angle. The bin size is 0.2 mm. The first four such events generated are shown.

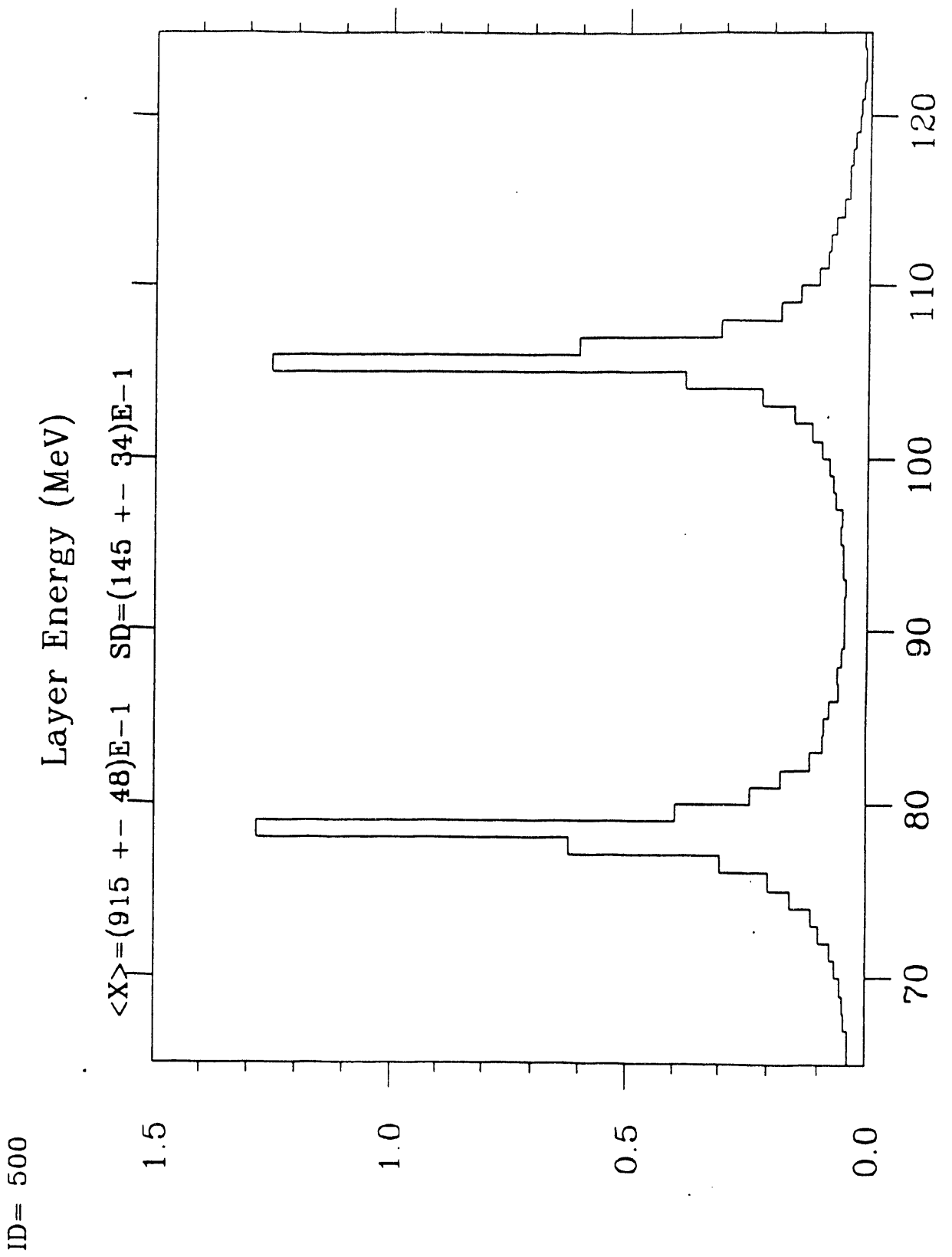

Figure 19
Same as Figure 17 but averaged over 500 events.

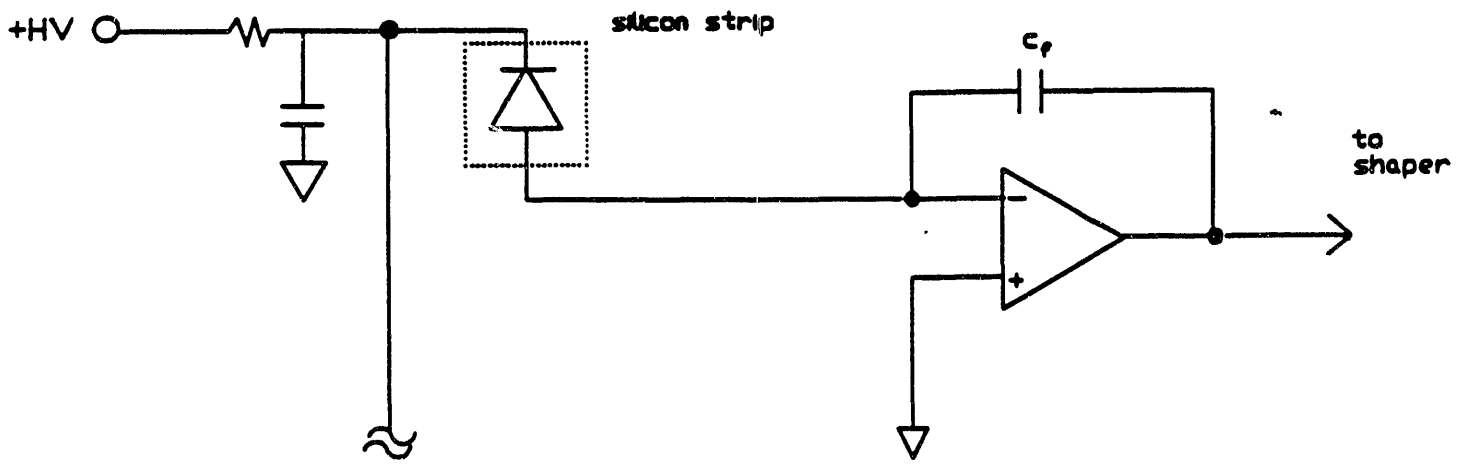

Figure 20
Principle of connection for each silicon detector element, represented here by a diode.

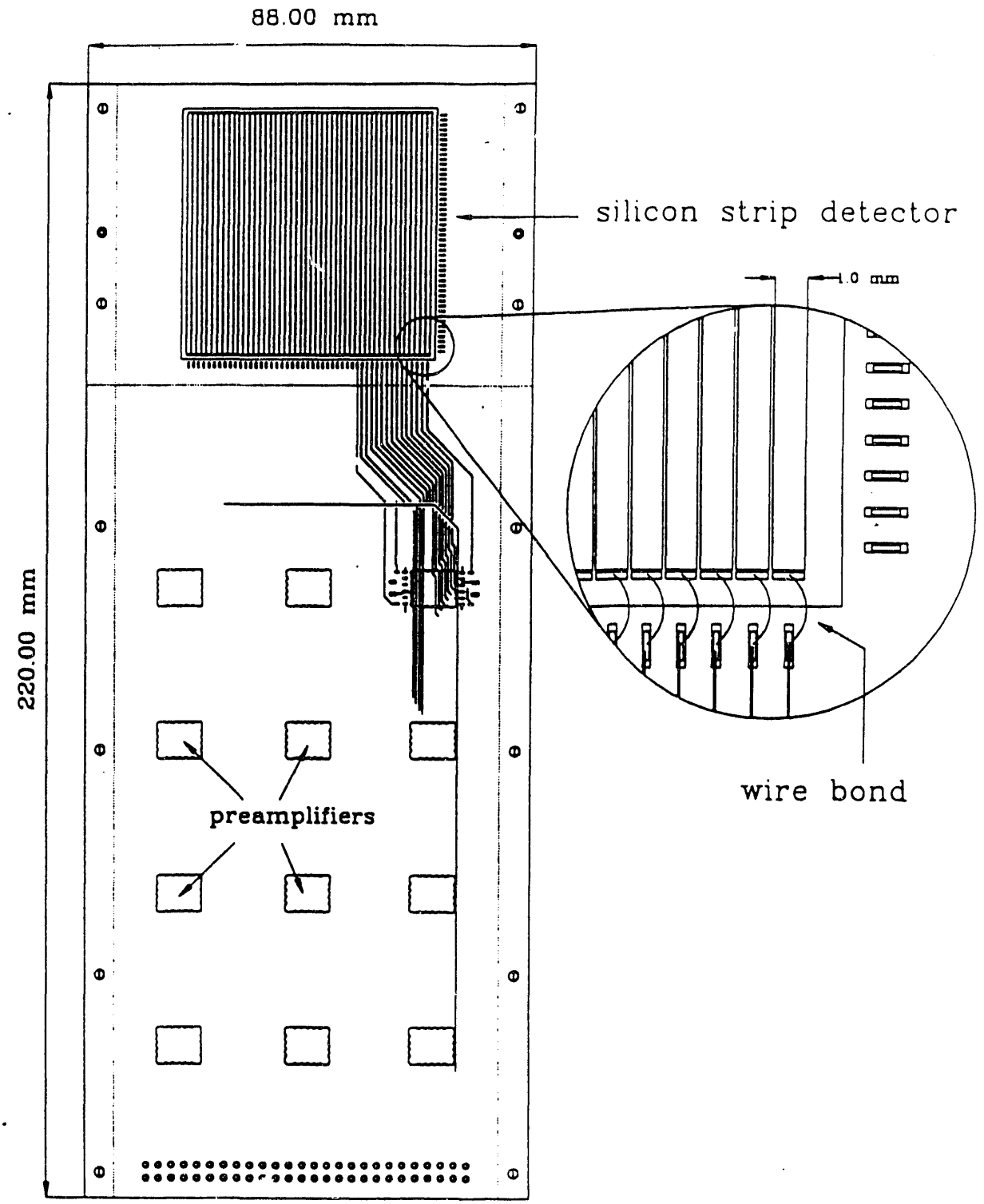

Figure 21
Drawing of the silicon detectors mounted on their readout board with preamplifier chips and output connectors. Wire bonding provided the connections between individual strips and the corresponding readout board trace.

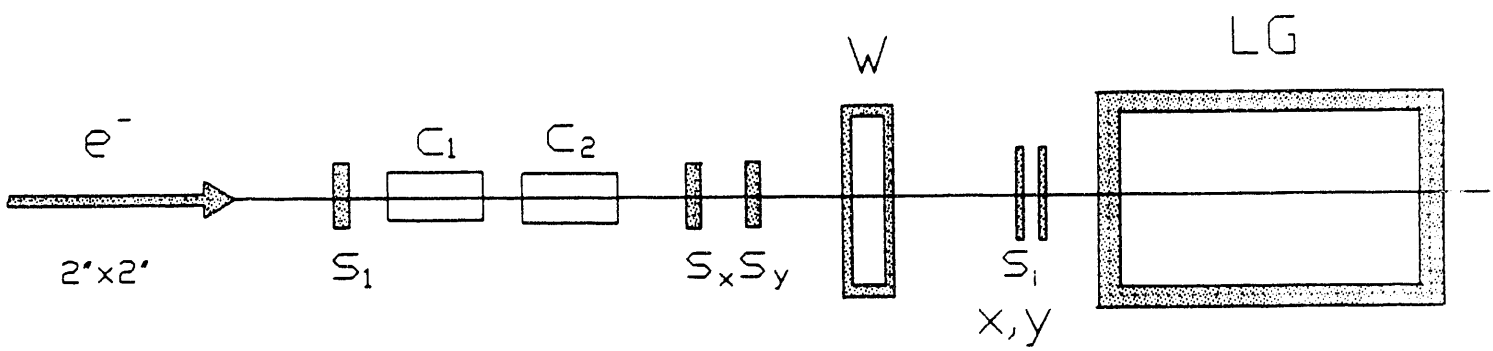

Figure 22
The test beam configuration in the A2 line at BNL.

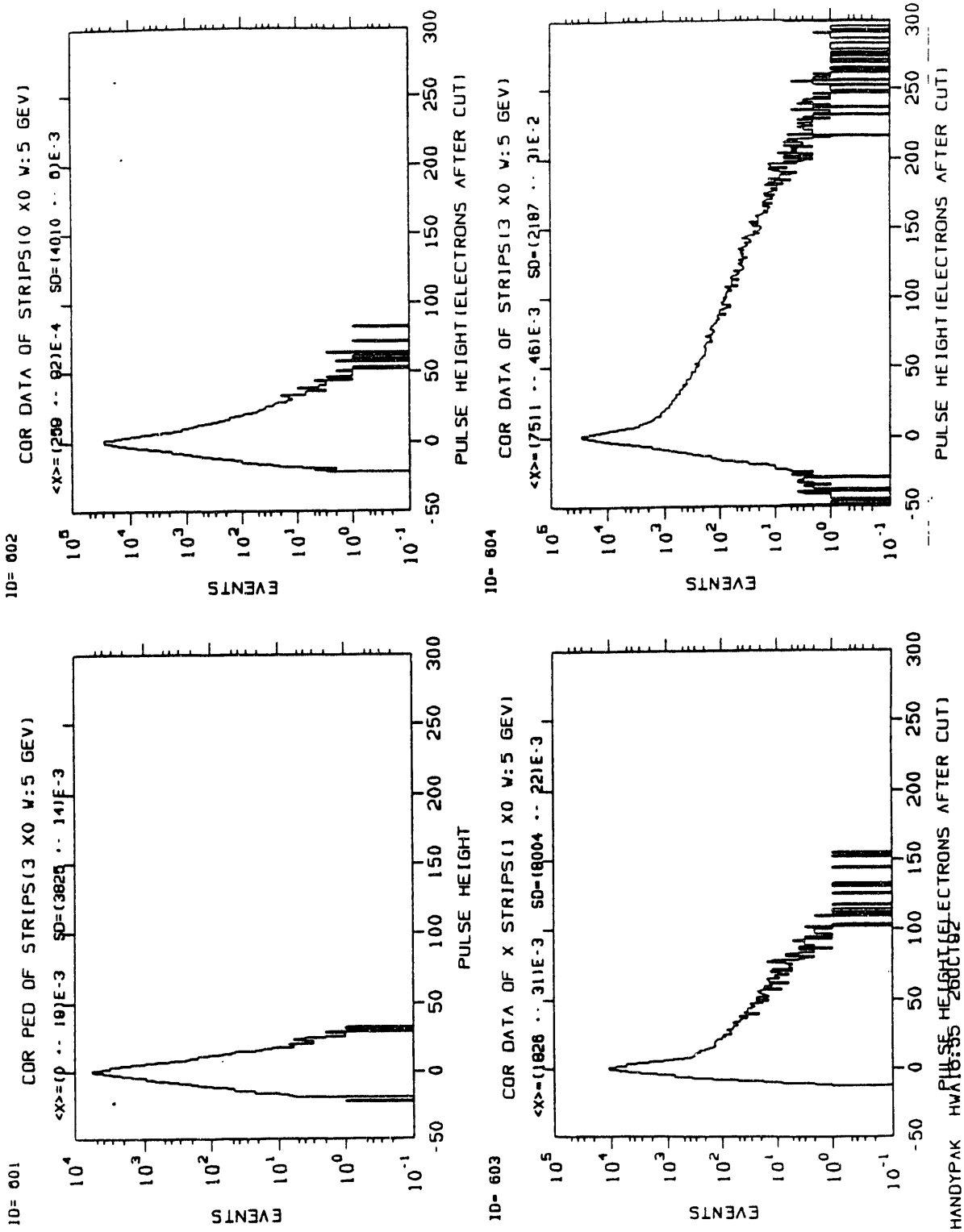

Figure 23

Pulse height distributions for all strips under different conditions: (a) pedestals only; 5 GeV with (b) no radiator, (c) 1 X_0 of tungsten, (d) 3 X_0 of tungsten.

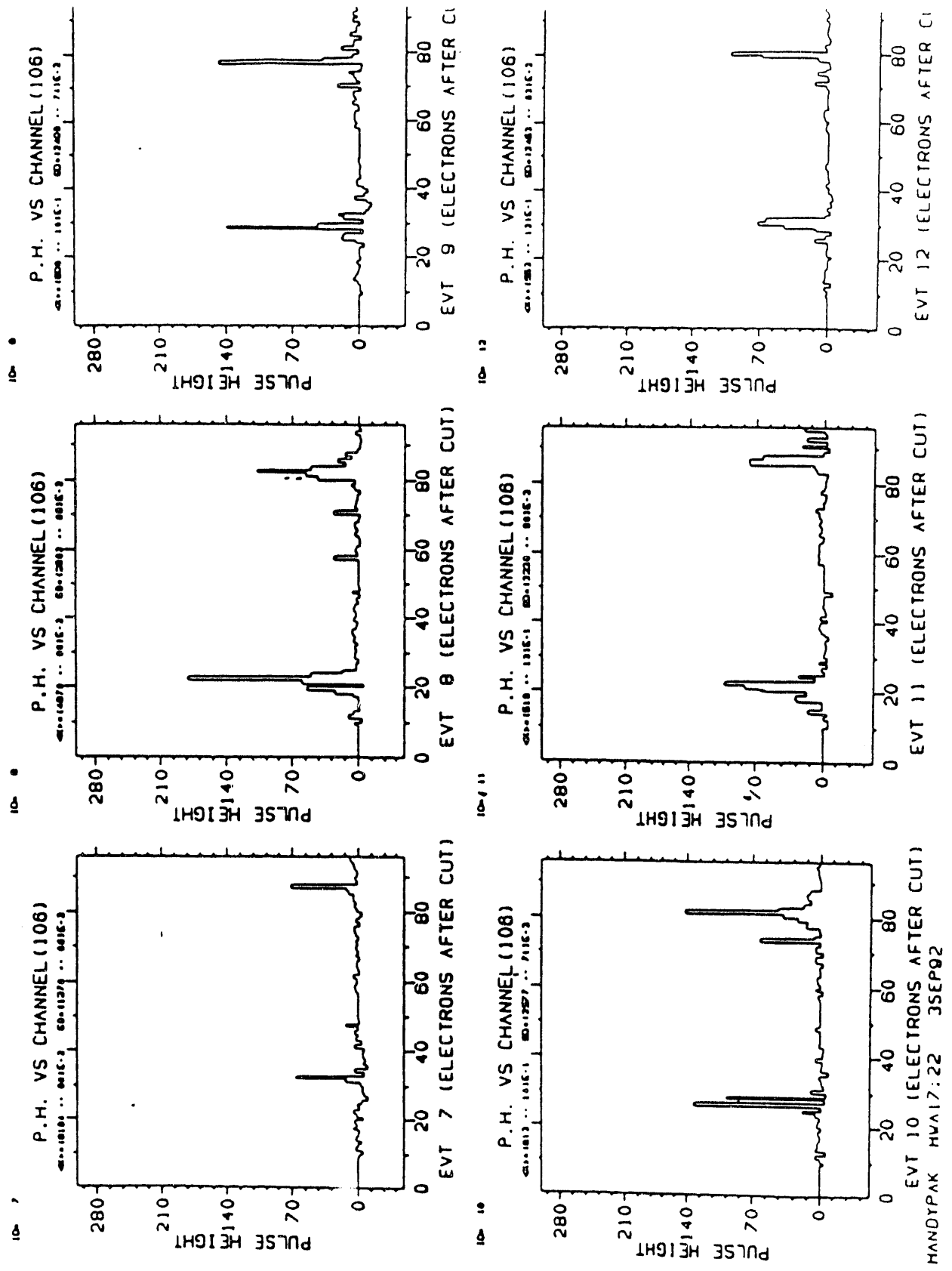

Figure 24 Event displays (pulse height versus strip number) for the first 6 events of a run with 5 GeV electrons and 3 X_0 of tungsten radiator. The first 48 strips are oriented in X and the second 48 strips in Y.

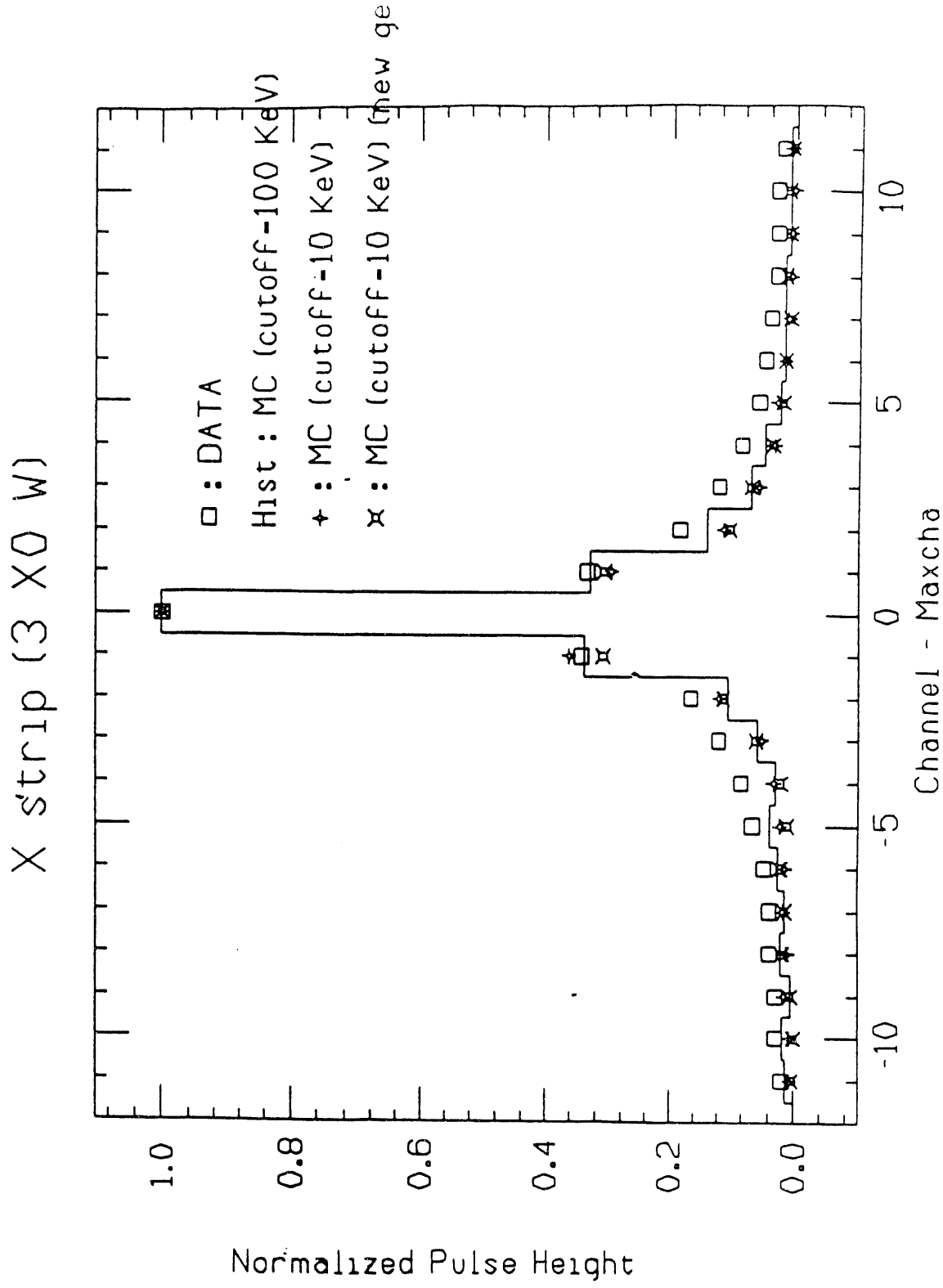

Figure 25

Transverse shower profile averaged over 2800 events for 5 GeV electons with 3 X_0 of tungsten radiator(squares). The histogram is the corresponding EGS simulation for 100 events.

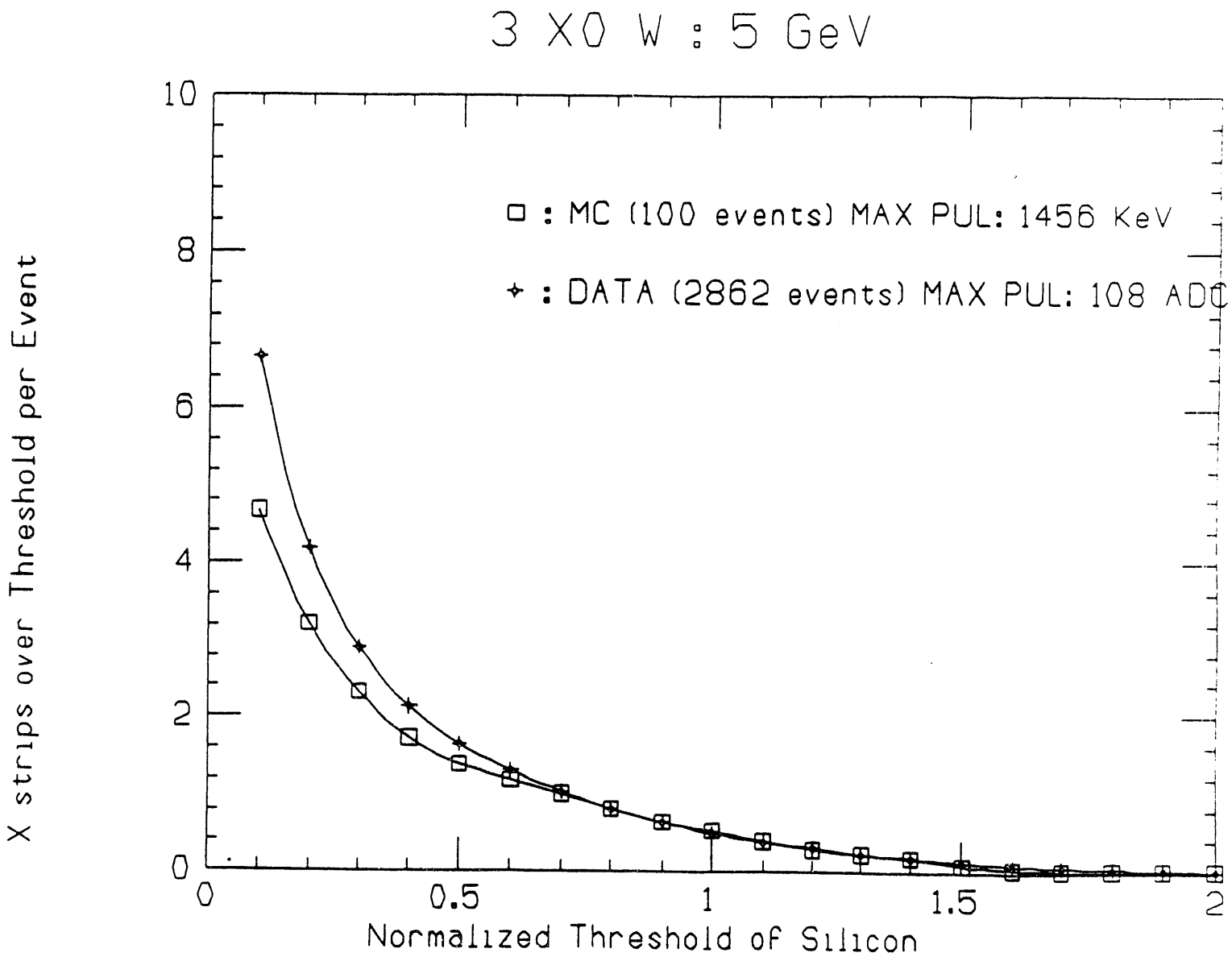

Figure 26
Distribution of number of strips over threshold as a function of that threshold for data and EGS simulation.

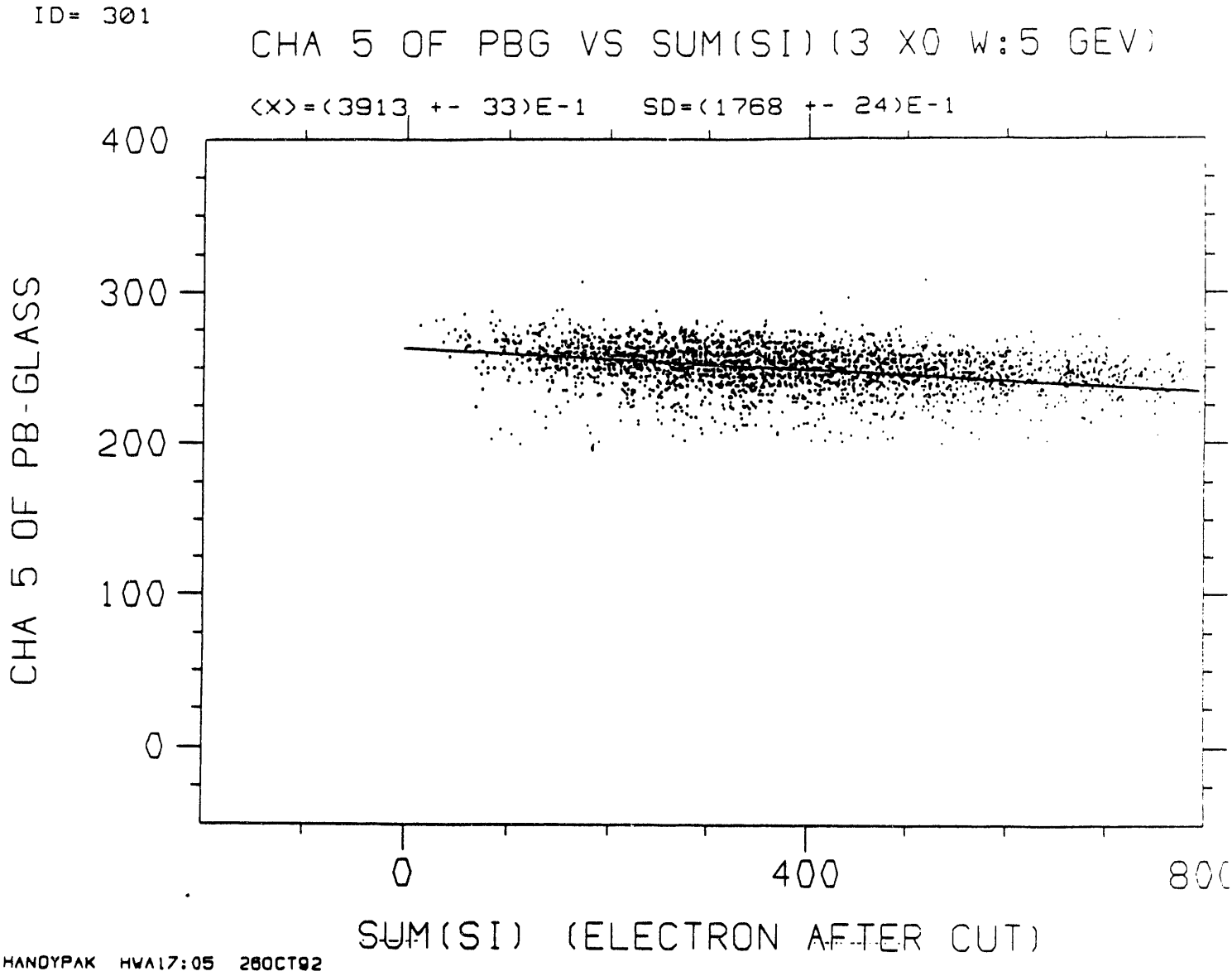

Figure 27

Scatter plot of total measured silicon energy versus measured lead glass energy. The line indicates the correlation between these quantities.

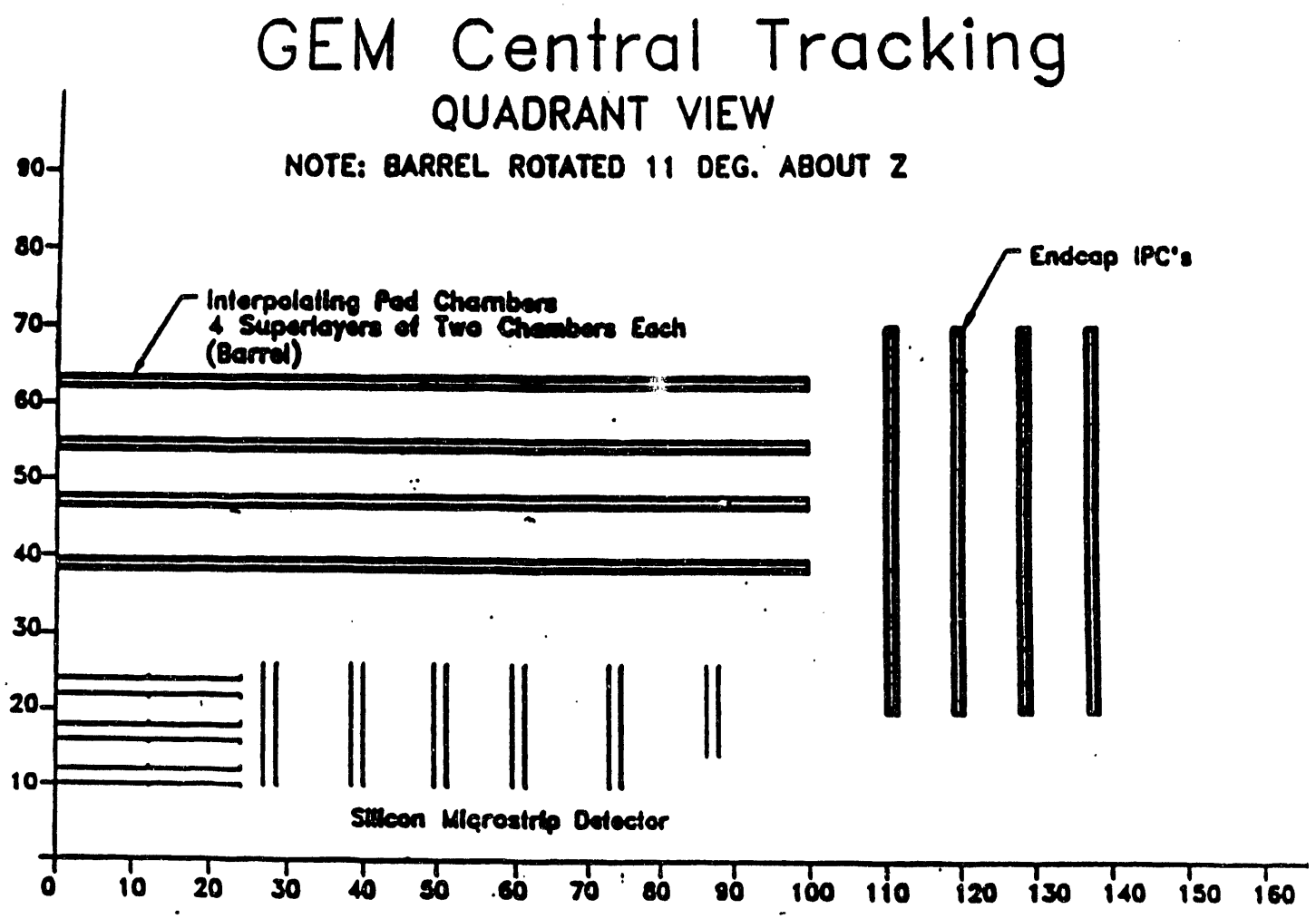
GEM Central Tracking
QUADRANT VIEW
NOTE: BARREL ROTATED 11 DEG. ABOUT Z
Interpolating Pad Chambers
4 Superlayers of Two Chambers Each
(Barrel)
Endcap IPC's
Silicon Microstrip Detector
90
80
70
60
50
40
30
20
10
0
10
20
30
40
50
60
70
80
90
100
110
120
130
140
150
160

Figure 28

GEM SILICON INNER TRACKER

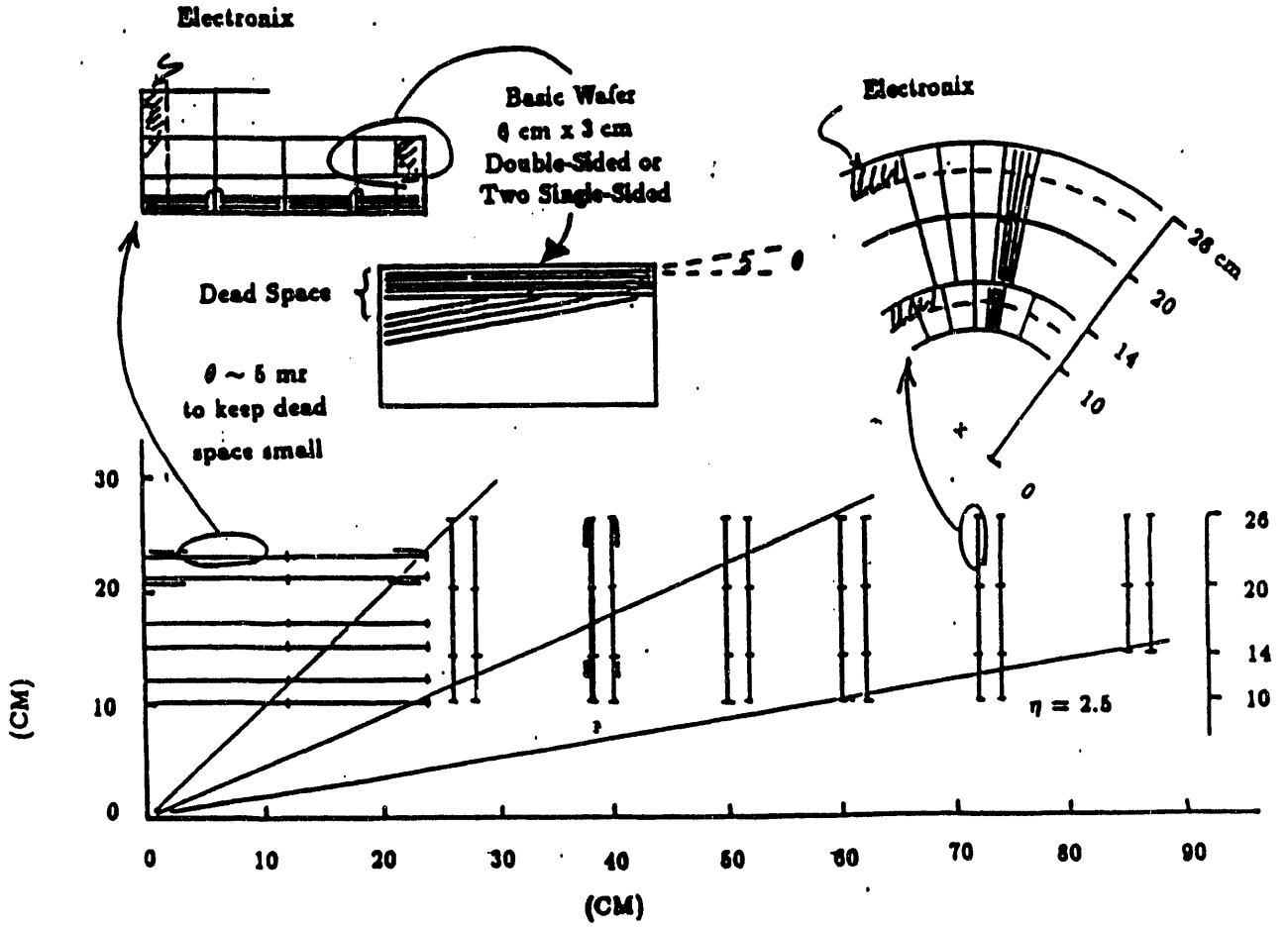

Figure 29

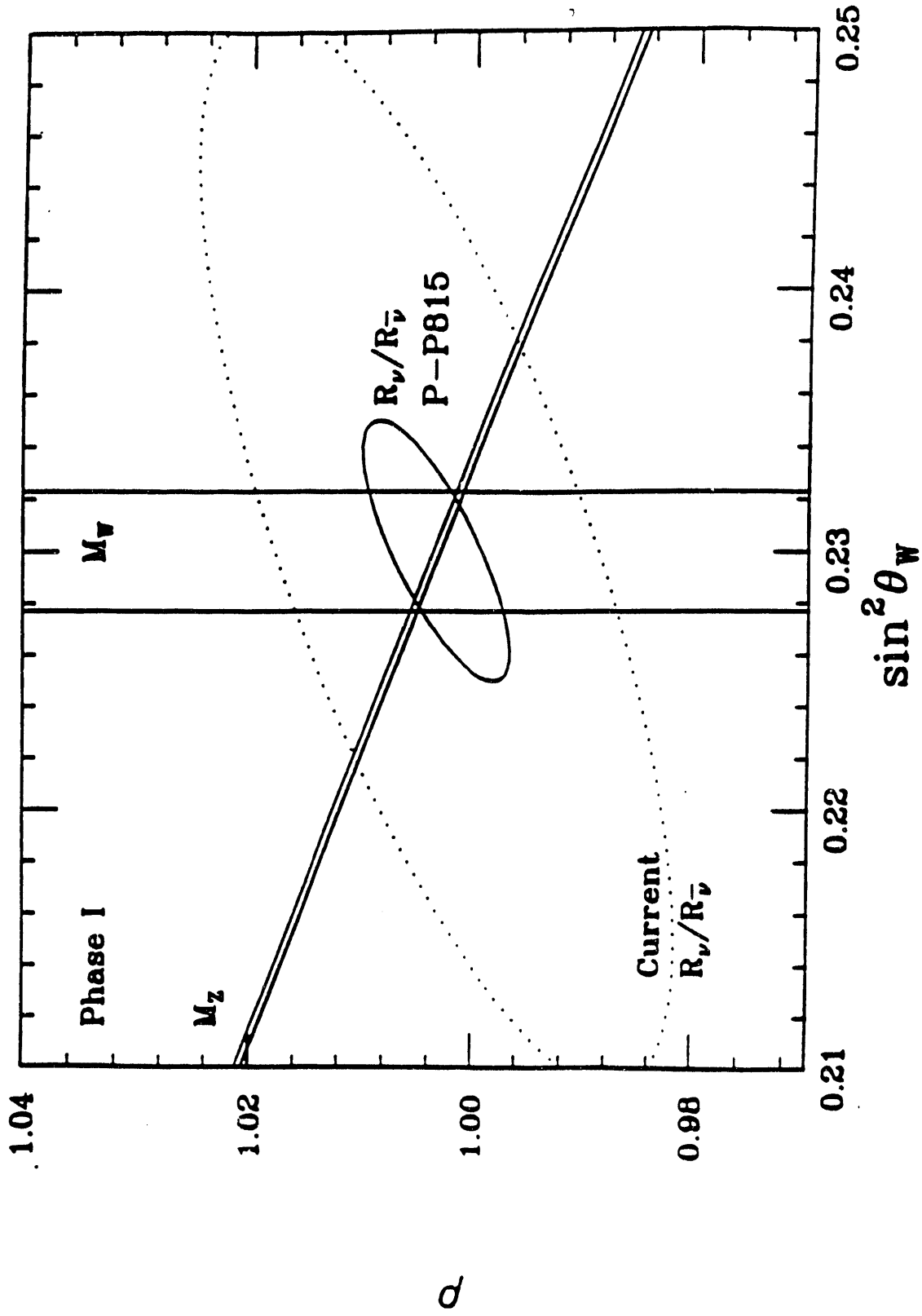

Figure 30
Expected error ellipse for E815 in the $\sin^2\theta_W - \rho$ plane compared to present νN results. Also shown are the allowed bands for the M_Z and M_W measurements.

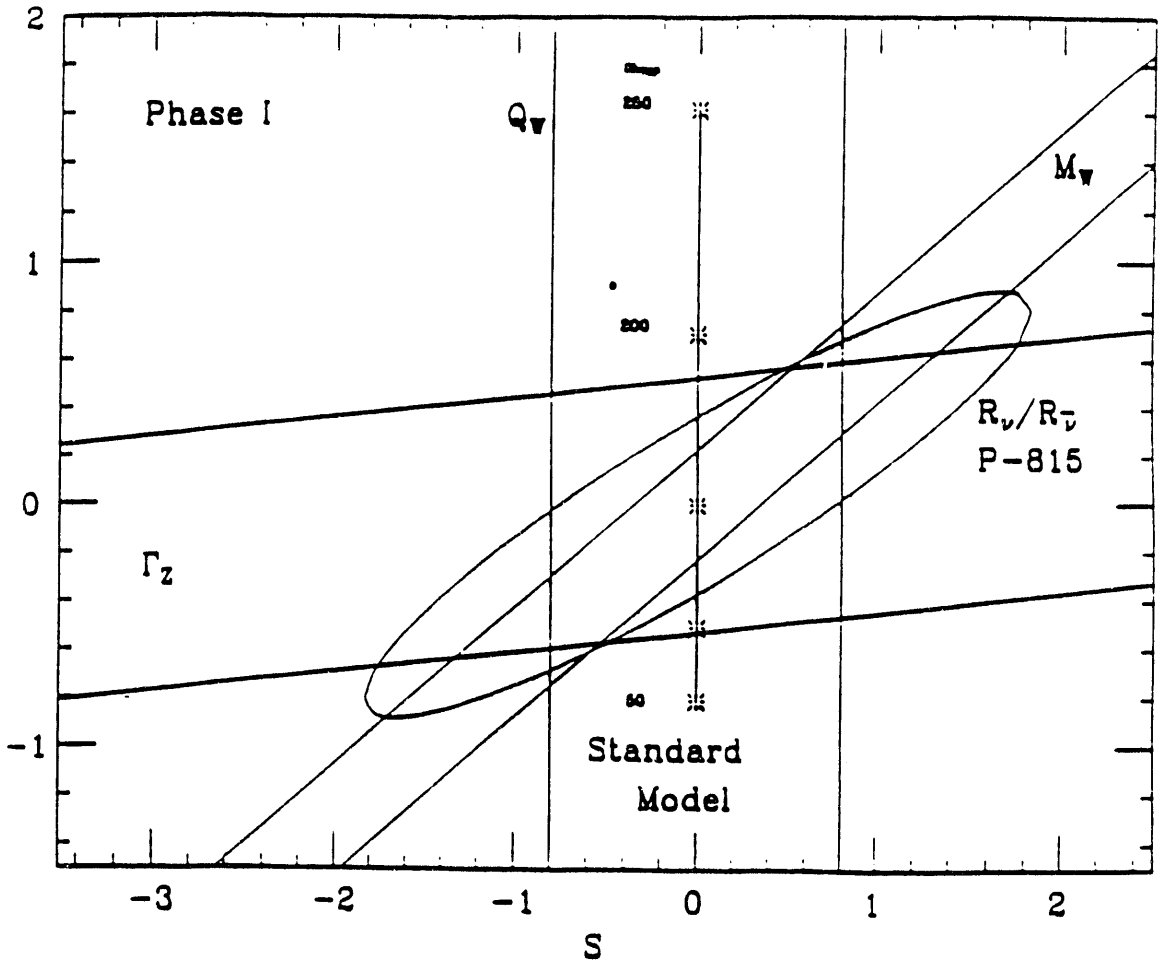

Figure 31
The expected E815 errors translated to the $S-T$ plane. The line at $S = 0$ is the Standard Model for different values of the top-quark mass, where $T = 0$ corresponds to $m_t = 140$ GeV/c^2.

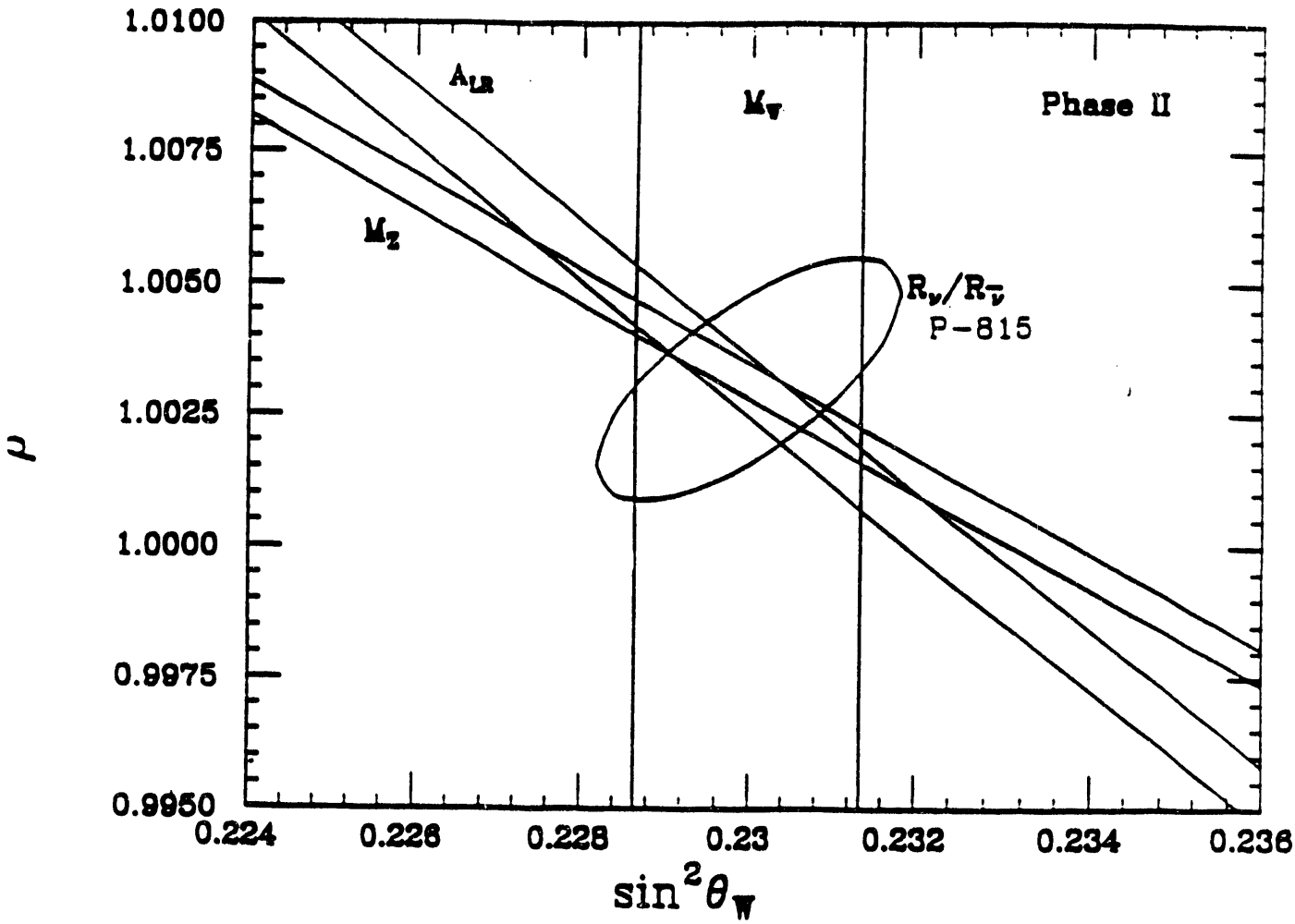

Figure 32
Same as Figure 30, but with errors expected for the late 1990's with a next generation E815 experiment ("Phase II").

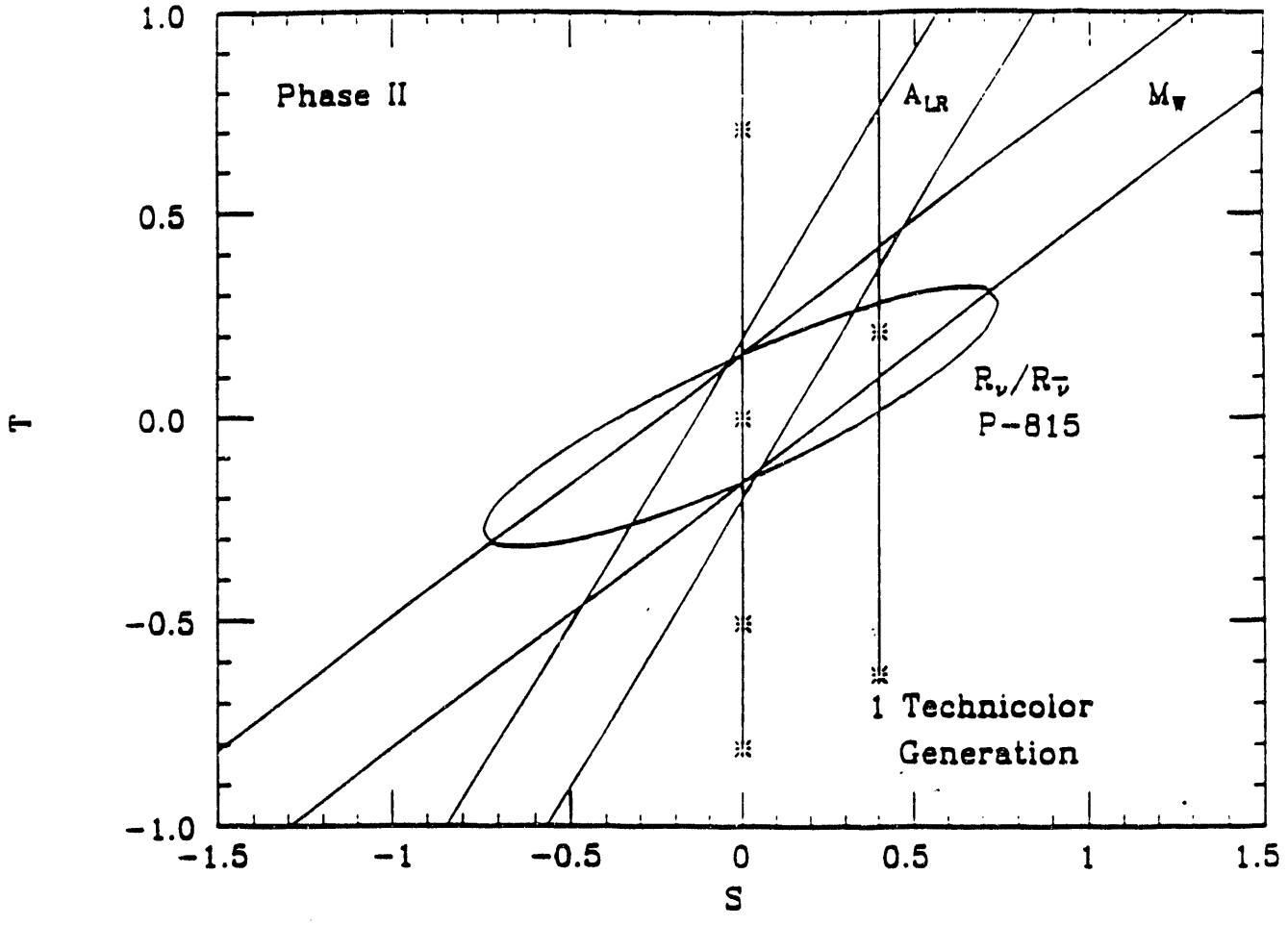

Figure 33
Same as Figure 31, but for Phase II errors.

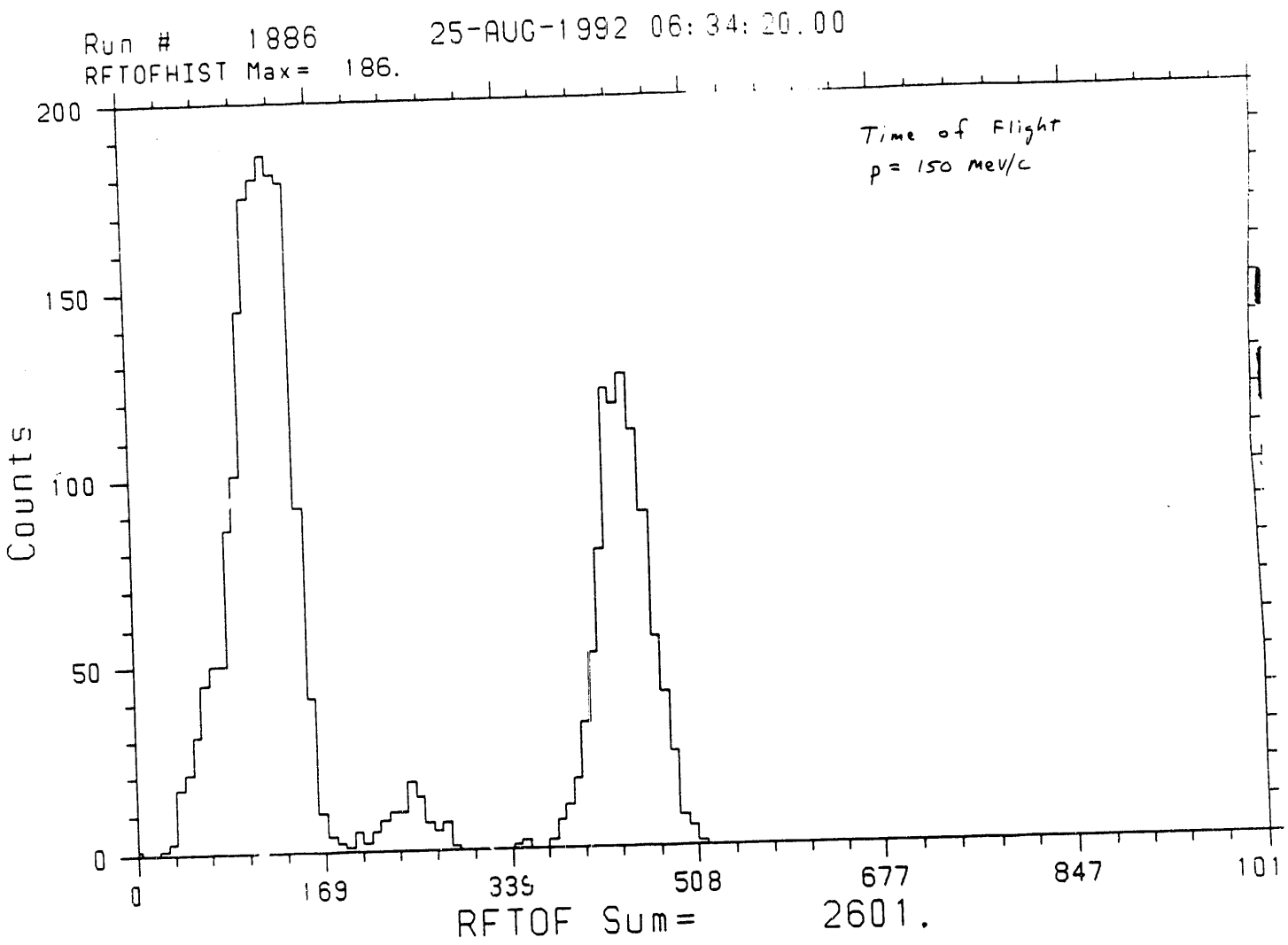

Figure 34

Time of flight data at $p = 150$ MeV/c. From left to right are clearly identifiable π, μ, and electron peaks.

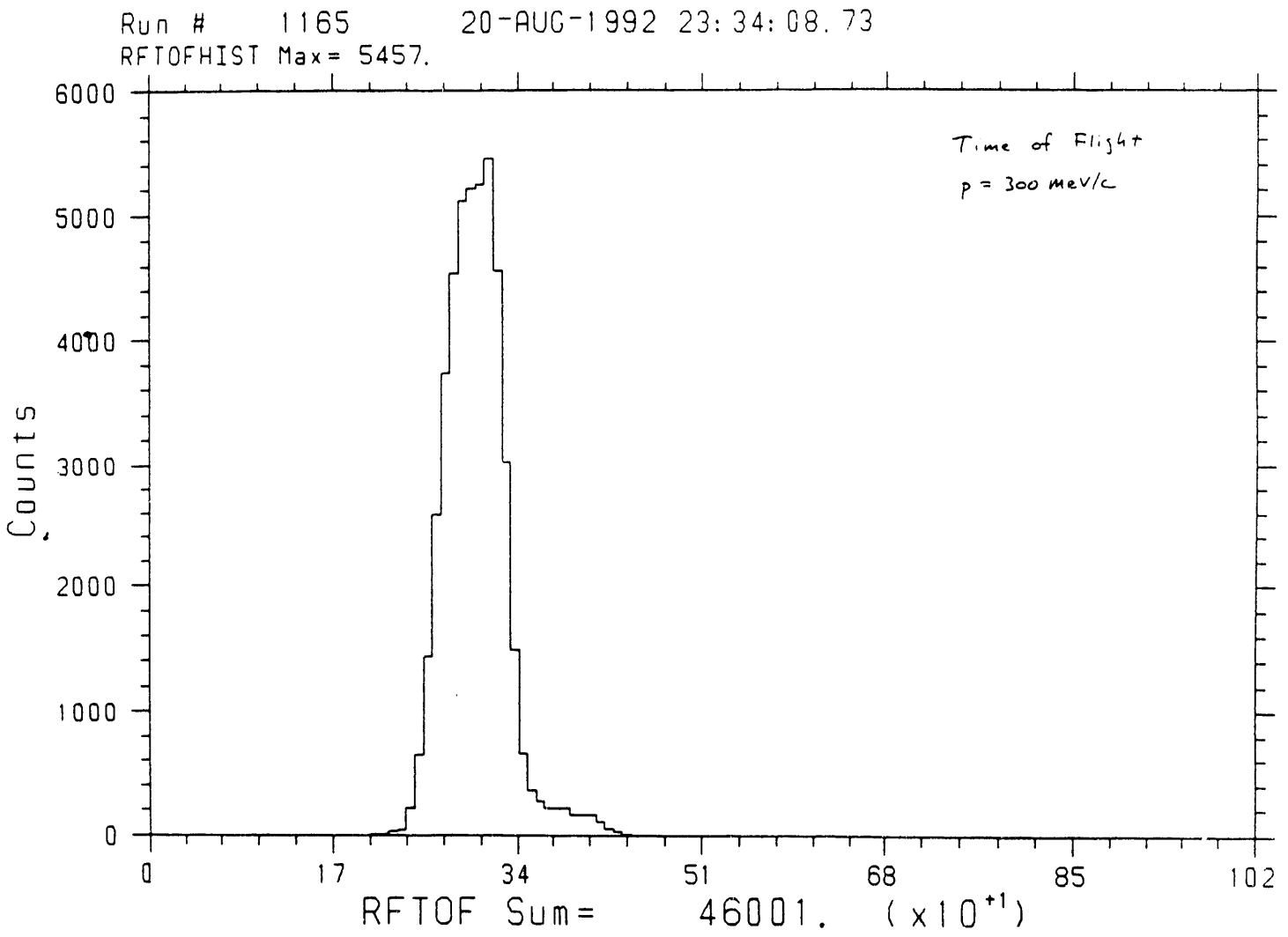

Figure 35

Time of flight data at p = 300 MeV/c. The electrons are now in the tail of the π distribution.

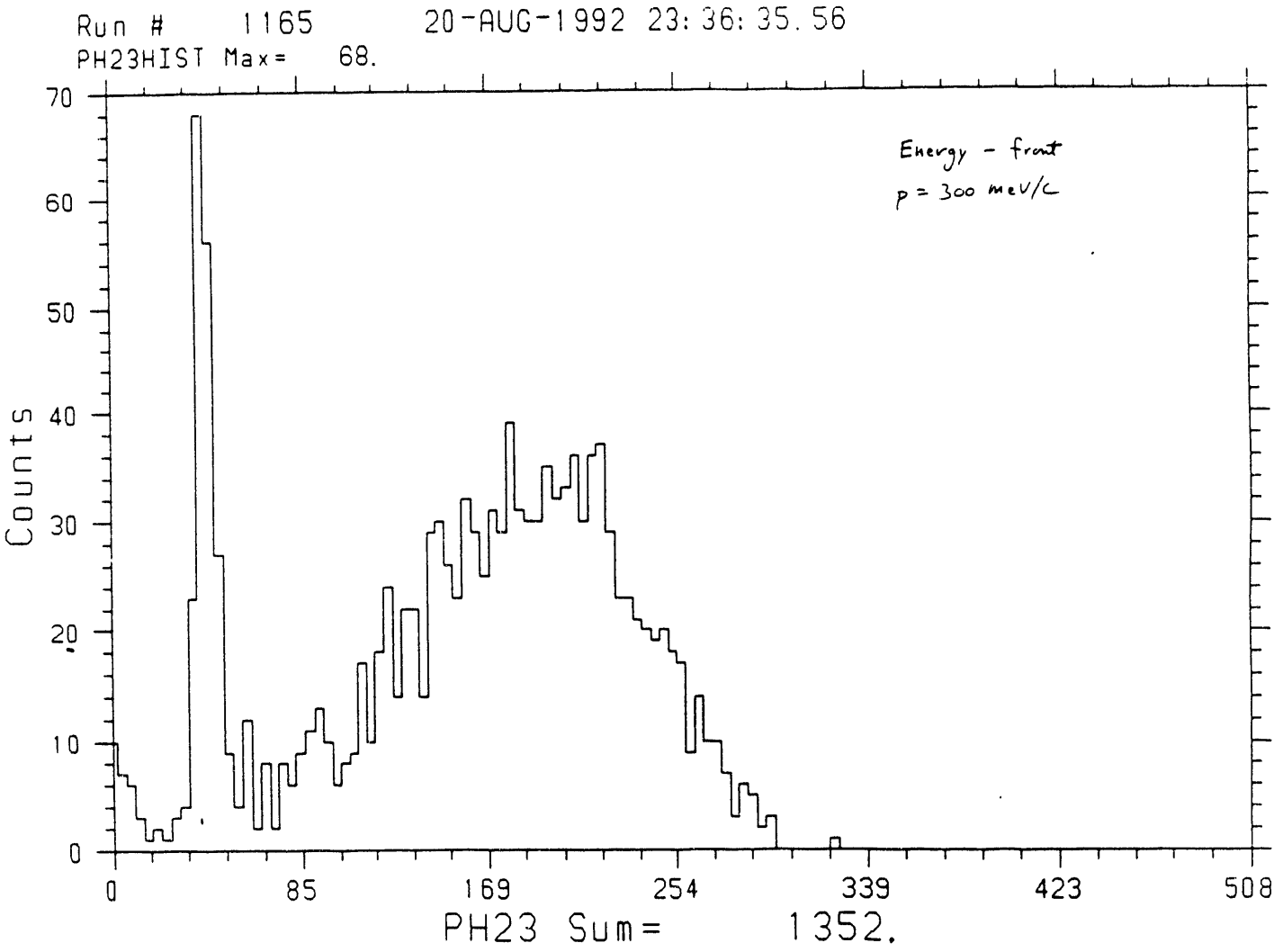

Figure 36
Measured energy (in MeV) in front crystal. $p = 300$ MeV/c. The beam is centered on the crystal. The narrow peak at ≈ 40 MeV is due to through-going charged pions.

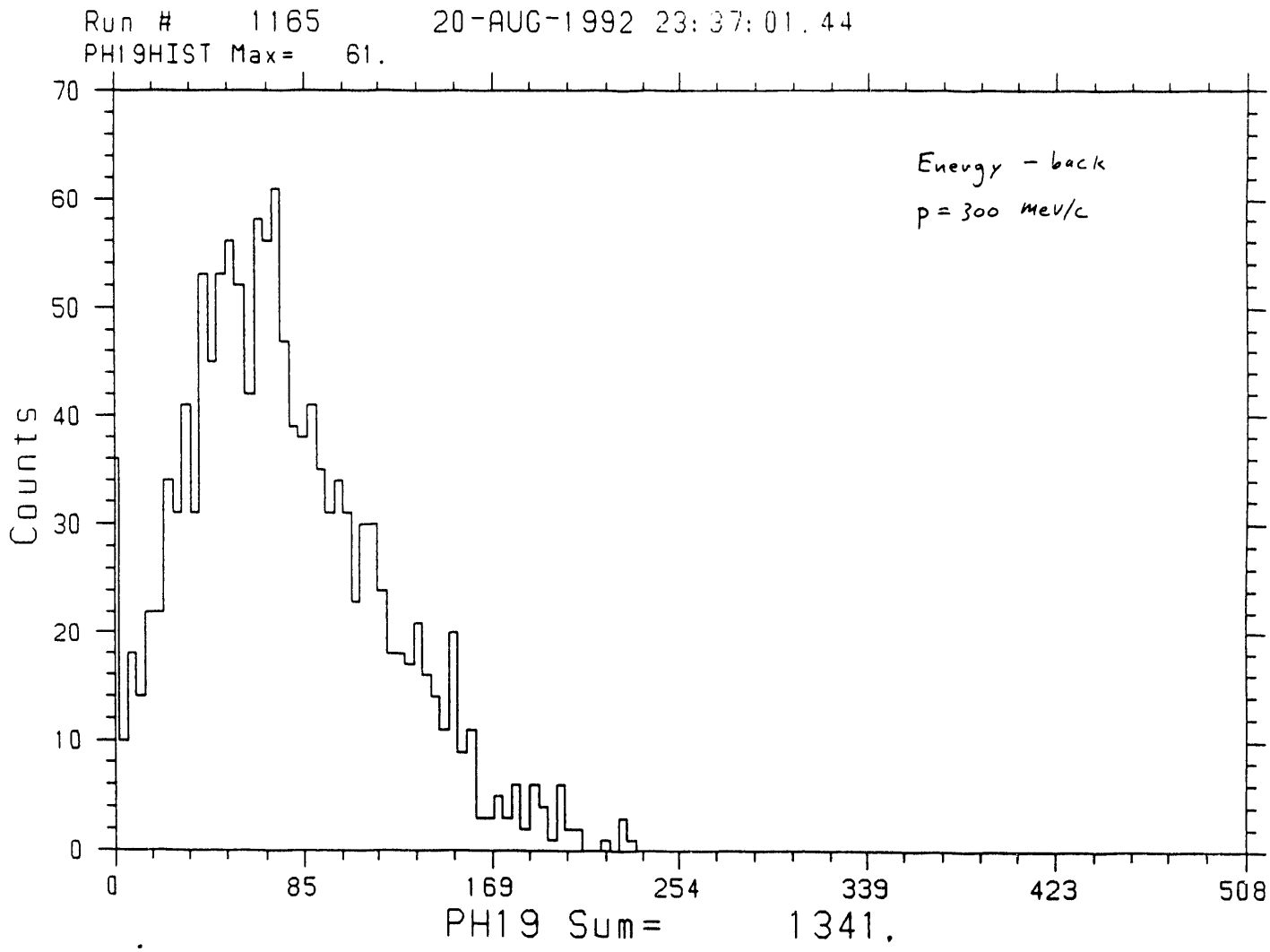

Figure 37
Same as previous figure, but for the back crystal.

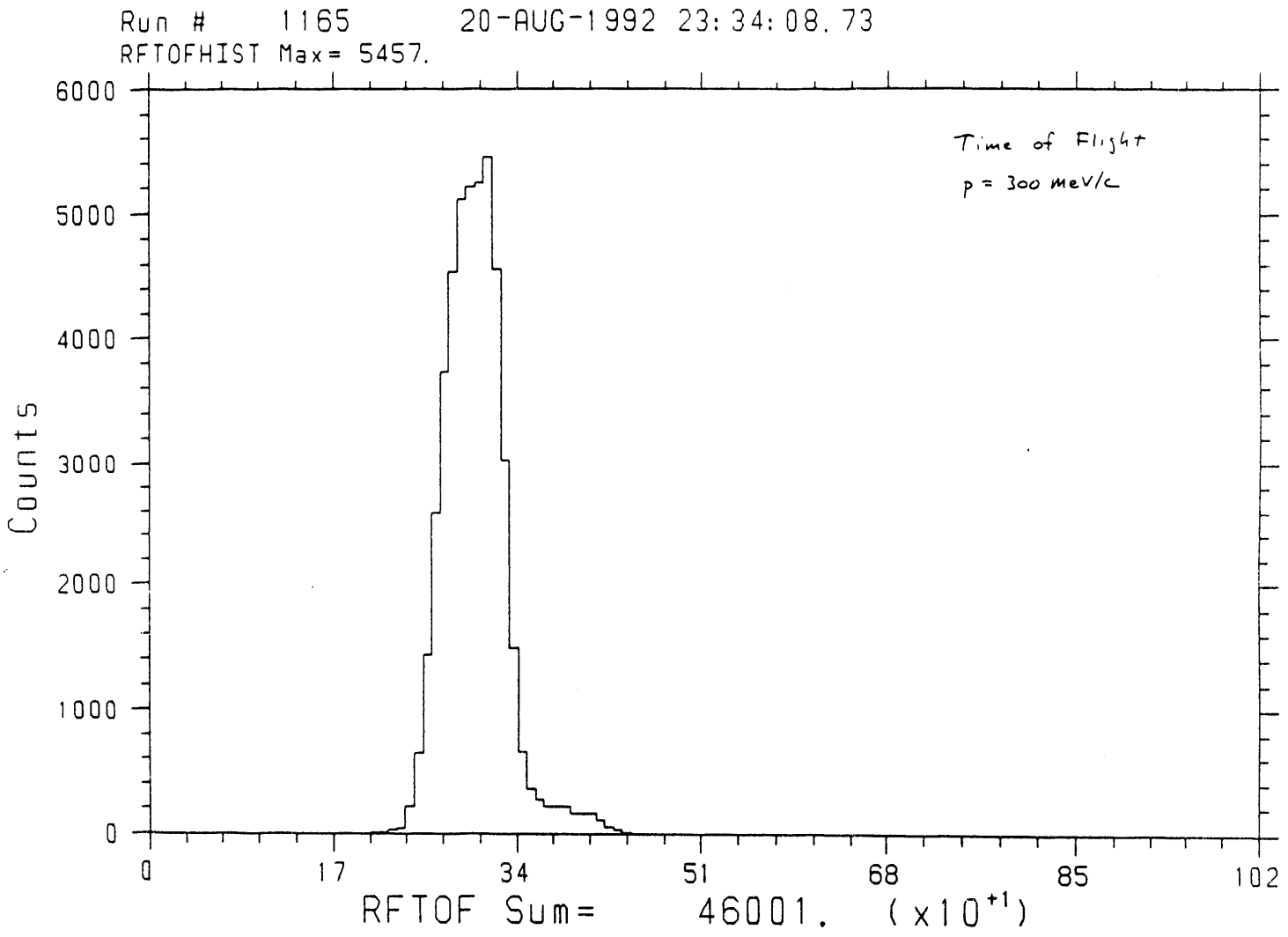

Figure 38

Sum of front and back energies (previous two figures). The low-energy tail is dominated by pion background.

END

DATE
FILMED
6/16/93